Personal Account

THE CHEMICAL RECORD

DOI: 10.1002/tcr.201800089

Material Design Concept of Lithium-Excess Electrode Materials with Rocksalt-Related Structures for Rechargeable Non-Aqueous Batteries

Naoaki Yabuuchi*[a, b]

Abstract: Dependence on lithium-ion batteries for automobile applications is rapidly increasing, and further improvement, especially for positive electrode materials, is indispensable to increase energy density of lithium-ion batteries. In the past several years, many new lithium-excess high-capacity electrode materials with rocksalt-related structures have been reported. These materials deliver high reversible capacity with cationic/anionic redox and percolative lithium migration in the oxide/oxyfluoride framework structures, and recent research progresses on these electrode materials are reviewed. Material design strategies for these lithium-excess electrode materials are also described. Future possibility of high-energy non-aqueous batteries with advanced positive electrode materials is discussed for more details.

Keywords: lithium, sodium, batteries, anionic redox

1. Development of Lithium-Ion Batteries with Stoichiometric Layered Oxides

In the past four decades, rechargeable lithium batteries (so-called lithium-ion batteries) were extensively studied, and now its technology was highly sophisticated after first commercialization in 1991. Now, more than a million of electric vehicles equipped with an electric motor and lithium battery have been sold per year in the global market. For a long time, the transportation system was depending on the technology of internal combustion engines. The lithium batteries are starting to substitute greener and sustainable energy resources for fossil fuels. Gravimetric energy density of the lithium batteries is 2–3 times greater when compared with batteries with aqueous electrolyte (*e.g.*, metal hydride batteries).[1] Nevertheless, the demand for further increase in energy density is still growing to reduce the size of batteries.

[a] *N. Yabuuchi*
Department of Chemistry and Life Science, Yokohama National University, 79-5 Tokiwadai, Hodogaya-ku, Yokohama, Kanagawa 240-8501, Japan
E-mail: yabuuchi-naoaki-pw@ynu.ac.jp
[b] *N. Yabuuchi*
Elements Strategy Initiative for Catalysts and Batteries, Kyoto University,
1-30 Goryo-Ohara, Nishikyo-ku, Kyoto 615-8245, Japan

The lithium batteries consist of two lithium insertion materials, *i.e.*, positive and negative electrode materials, which reversibly store both lithium ions and electrons on charge/discharge processes.[2] The first generation of lithium batteries consisted of $LiCoO_2$[3] and carbonaceous materials as positive and negative electrode materials, respectively. A theoretical capacity of $LiCoO_2$ is calculated from the following reaction;

$$LiCoO_2 \rightarrow \square CoO_2 + Li^+ + e^- \quad (1)$$

Herein, $\square$ denotes vacancy created by lithium extraction in the host structure. A trivalent Co ion as cationic species in $LiCoO_2$ is oxidized to a tetravalent state, and lithium ions are extracted from the host structure to maintain charge neutrality. Theoretical capacity of $LiCoO_2$ is calculated to be 274 $mAh\,g^{-1}$ from the equation 1 (a practical reversible capacity is limited to ~200 $mAh\,g^{-1}$). $LiCoO_2$ is still widely used in state-of-the-art lithium-ion batteries, especially for portable electronic devices because of high volumetric energy density.

For electric vehicle applications, $LiMn_2O_4$ and its derivatives, whose crystal structure is classified as a spinel-type structure, were used as positive electrode materials. For $LiMn_2O_4$, MnO_6 octahedra share edges, forming a three-dimensional framework structure, in which Li ions are located

 © 2019 The Chemical Society of Japan & Wiley-VCH Verlag GmbH & Co. KGaA, Weinheim

at tetrahedral sites (Figure 1). Nearly all of Li ions are reversibly extracted from the crystal structures as a 4-volt class electrode material without the destruction of the framework structure. However, a reversible capacity is limited to ~120 mA h g^{-1} as shown in Figure 1, and available energy density is limited to 450–500 Wh kg^{-1} on the basis of metallic lithium. To increase the energy density, Ni-based layered materials are now used for electric vehicles. Typical charge/discharge curves of stoichiometric $LiNiO_2$ are also shown in Figure 1. A crystal structure of stoichiometric $LiMO_2$ (M = transition metal ions) is classified as a rocksalt-related layered structure with the cubic close-packed (ccp) lattice of oxide ions. Li and M ions are ordered into alternate layers perpendicular to [111] of the original rocksalt lattice, forming the layered structure with a rhombohedral lattice. $LiCoO_2$ and $LiNiO_2$ are isostructural, leading the formation of solid solution in the entire composition, $LiCo_xNi_{1-x}O_2$ ($0 \leq x \leq 1$).[4] A reversible capacity of stoichiometric $LiNiO_2$ exceeds 200 mA h g^{-1} even though operating voltage is slightly lowered compared with the spinel-type manganese oxide. Energy density as positive electrode materials reaches 700–750 Wh kg^{-1}. Since stoichiometric $LiNiO_2$ is thermally unstable after charge,[5–7] other transition metal ions are partially substituted for nickel ions. The Co/Al-substituted system, $LiNi_{0.8}Co_{0.15}Al_{0.05}O_2$,[8] is currently used for practical applications. In addition, the Mn/Co-substituted system was also extensively studied as positive electrode materials.[9–12] Charge/discharge curves of $LiNi_{0.8}Mn_{0.1}Co_{0.1}O_2$ are also compared with stoichiometric $LiNiO_2$ in Figure 1. Average operating voltage is slightly higher than the pure Ni system, and voltage plateaus associated with phase transitions are less pronounced for $LiNi_{0.8}Mn_{0.1}Co_{0.1}O_2$. Metal substitution disturbs lithium/charge ordering in the layered structure.[13] Although the Ni-based layered materials are currently used for electric vehicles, available energy density is restricted below 800 Wh kg^{-1} based on metallic lithium. The development of high-capacity positive electrode materials, which outperform the Ni-based layered materials, is indispensable to further increase energy density of commercial lithium-ion batteries.

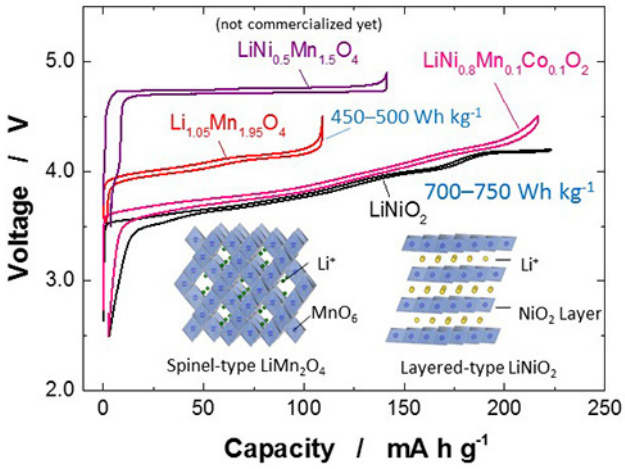

Figure 1. Comparison of charge/discharge curves of representative lithium insertion materials used as positive electrode materials for lithium-ion batteries. Schematic illustrations of spinel-type and layered-type oxides are also compared in the inset.

2. Material Design Concept of Li-Excess Rocksalt Oxides

Since theoretical capacities of positive electrode materials depend on lithium contents in the host structure, substitution of lithium ions for transition metal ions in $LiMO_2$ ($Li_{1+x}M_{1-x}O_2$) is important strategy to design high-capacity positive electrode materials. In the past decade, Li-enriched materials, Li_2MO_3-type layered materials ($M = Mn^{4+}$, Ru^{4+} and other tetravalent ions), which are also classified as the cation-ordered rocksalt-type structure,[14] have been extensively studied as potential high-capacity electrode materials.[15–23] Both compositions are found in a Li–M–O triangular phase diagram on a rocksalt tie-line shown in Figure 2. Li_2MO_3 is reformulated as $Li_{4/3}M_{2/3}O_2$ when the oxygen content in the chemical formula is normalized to two. Since the lithium content is enriched from conventional layered materials, these oxides are often called *"lithium-excess"* and *"lithium-rich"* materials. Among the Li_2MO_3-type oxides, a Mn-system, Li_2MnO_3 and its derivatives have been the most widely studied as electrode materials. A theoretical capacity of Li_2MnO_3 is calculated from the following reaction;

Naoaki Yabuuchi is a professor at Yokohama National University. He completed his PhD at Osaka City University in 2006 and his postdoc at MIT, with research expertise in the development of new electrode materials and study on reaction mechanisms for high energy Li/Na batteries. He has over 90 publications in these areas. He is the recipient of First International Award, "Science Award Electrochemistry" by Volkswagen and BASF, The 2nd ISSI Young Scientist Award, and ISE Prize for Applied Electrochemistry, The Young Scientists' Prize from the Minister of Education, Culture, Sports, Science and Technology, Japan among other honors.

 © 2019 The Chemical Society of Japan & Wiley-VCH Verlag GmbH & Co. KGaA, Weinheim

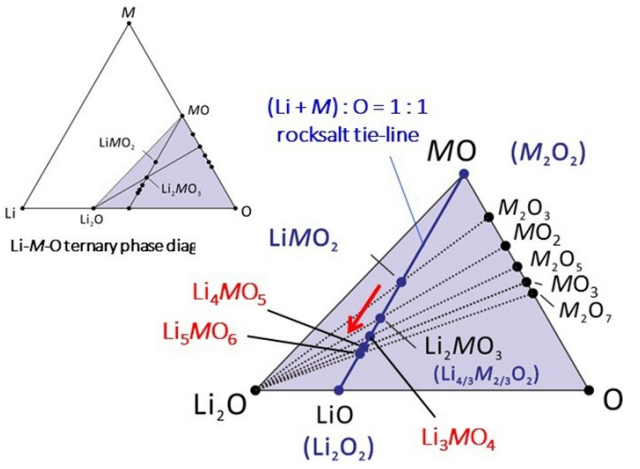

Figure 2. A Li–*M*–O triangular phase diagram, and its expanded view is also shown. Many cation ordered/disordered rocksalt phases are located on a tie-line (solid blue line) between *M*O and LiO. As increase in lithium contents in the structure, oxidation states of *M* ions increase along this tie-line; see also Figure 3.

$$Li_2MnO_3 \rightarrow \square_2MnO_3 + 2Li^+ + 2e^- \quad (2)$$

A theoretical capacity is calculated to be 459 mA h g^{-1} when two electrons and lithium ions are successfully and reversibly extracted from the host structure. This value is much higher than those of stoichiometric layered oxides. Nevertheless, for a long time, Li_2MnO_3 was regarded as electrochemically inactive because of difficulty of oxidation of tetravalent Mn ions into higher oxidation states. However, the fact is that Li_2MnO_3 is electrochemically active associated with the contribution of anions (oxide ions) for the charge compensation process.[18,20] Detailed reaction mechanisms of Li_2MnO_3 are found in the literature.[24] Historically, charge compensation by non-cationic species has been already known in sulfides before 1990.[25] Sulfide ions are relatively soft and easily polarizable, and oxidation of sulfide ions (S^{2-}) and the formation of disulfide (persulfide) ions (2 S^{2-}) is a well-known process in many chemical/biological processes. Ligand hole stabilization has been also known associated with charge transfer from the oxide ion to the transition metal ions for a heavily hybridized system with oxygen 2p orbital, for example Fe^{4+} in $SrFeO_3$.[26] Similarly, the possibility of charge transfer from oxygen 2p to Co^{4+} in Li_xCoO_2 was also discussed in 1999.[27] If such ligand holes are directly and/or indirectly created by the electrochemical oxidation for the lithium-excess system, this process is classified as "*anionic*" redox.

Although a crystal structure of Li_2MnO_3 is essentially the same with $LiCoO_2$ (a difference is only found in additional lithium ions in transition metal layers as shown in Figure 3). Further enrichment of lithium contents in the structure is also possible by combining transition metals ions with higher transition metal ions. For instance, Li_3NbO_4 with pentavalent niobium ions,[28] Li_4MoO_5 with hexavalent molybdenum ions,[29] and Li_5ReO_6 with heptavalent rhenium ions[30] are found in the literature. These oxides are also classified as cation-ordered rocksalt-type structures (Figure 3) with the common ccp lattice of oxide ions, and found in the rocksalt tie-line in Figure 2. Although niobium and molybdenum as 4d-transition metal ions and rhenium as 5d-transtion metal ions are heavier ions, theoretical capacities of these oxides are attractive as electrode materials as summarized in Table 1. These transition metal ions with high oxidation states and lithium ions are located at octahedral sites in the ccp lattice of oxide ions, but arrangement of these ions are different from each other as shown in Figure 3. The theoretical capacity reaches 526 mA h g^{-1} for Li_4MoO_5 when anionic redox is utilized. However, these lithium-excess materials consist of transition metal ions without conductive d-electrons and are essentially insulators and/or semiconductors. Therefore, anionic redox reaction cannot be activated. Lithium insertion materials require both high ionic and electronic conductivity.

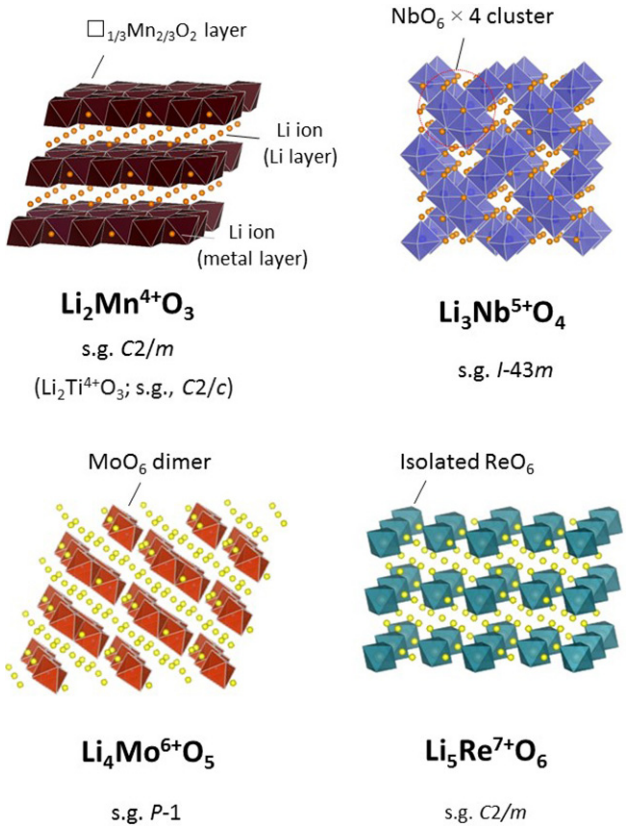

Figure 3. Schematic illustrations of the crystal structures of different lithium-excess oxides; Li_2MnO_3, Li_3NbO_4, Li_4MoO_5, and Li_5ReO_6. These illustrations were drawn using VESTA program.[85]

 © 2019 The Chemical Society of Japan & Wiley-VCH Verlag GmbH & Co. KGaA, Weinheim

Table 1. Comparison of theoretical capacity on the basis of lithium contents in structures for different lithium-excess materials.

$LiCoO_2$	Li_2MnO_3	Li_3NbO_4	Li_4MoO_5	Li_5ReO_6
274 mA h g^{-1}	459 mA h g^{-1}	452 mA h g^{-1}	526 mA h g^{-1}	423 mA h g^{-1}

To induce electronic conductivity, partial substitution of transition metals for these oxides is the effective strategy to design high-capacity positive electrode materials. Two possible scenarios for metal substitutions are shown in Figure 4. Since Li_3NbO_4 (similarly reformulated as $Li_{1.5}Nb_{0.5}O_2$), layered/rocksalt $LiMO_2$, with trivalent transition metal ions (Mn^{3+}, Fe^{3+}, V^{3+} *etc.*), and rocksalt *M*O with divalent transition metal ions (Ni^{2+}, Co^{2+}, Fe^{2+} *etc.*) have the common ccp lattice of oxide ions, the formation of solid solution among these phases is anticipated. Theoretical capacities calculated with *M* = Mn are also plotted in Figure 4 as hypothetical materials. Here, theoretical capacities are calculated on the basis of the pure anionic redox (red lines, which also correspond to the highest reversible capacities in the entire composition) and one-, two-, and three-electron redox with cationic species (blue lines). For the case of divalent metal substitution, a large reversible capacity cannot be obtained for one-electron redox reaction for cationic species. A theoretical reversible capacity is limited to ~200 mA h g^{-1}, indicating that the use of anionic redox and/or more than two-electron redox for cationic redox is required to design high-capacity electrode materials. For the case of trivalent metal substitution, since lithium contents in the structure remain high enough in the entire composition, more flexible material designs are possible in this system. Therefore, high-theoretical capacities, over 300 mA h g^{-1}, are expected with different material design strategies for both anionic/cationic redox as shown in the latter sections.

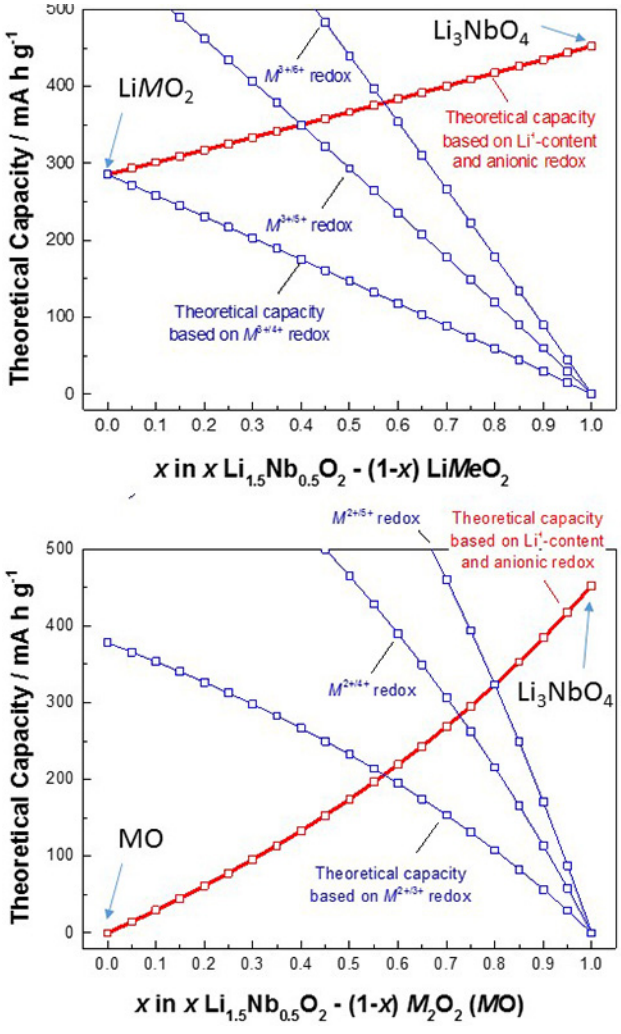

Figure 4. Theoretical capacity for Li_3NbO_4–$LiMO_2$ (top) and Li_3NbO_4–*M*O (bottom) binary systems. See the text for more details. The same oxygen contents ($Li_{1.5}Nb_{0.5}O_2$, $LiMO_2$, and M_2O_2) are used in the calculation for simplicity.

3. Li_3NbO_4- and Li_2TiO_3-Based Systems; Reversible and Irreversible Anionic Redox

Although pure Li_3NbO_4 is electrochemically inactive, the substitution of 3*d* transition-metal ions for Nb/Li ions effectively induces conductive electrons as mentioned above.[31,32] Such 3*d* transition-metal ions can accept electrons from oxide ions, leading to the activation of anionic redox coupled with cationic redox. After metal substitution, cation ordering observed for pure Li_3NbO_4 is lost, and a cation-disordered rocksalt-type structure is formed. Historically, cation-disordered rocksalt oxides was regarded as electrochemically inactive as electrode materials because of absence of Li migration path in a bulk structure.[33–35] Nevertheless, facile lithium migration is possible for lithium-excess cation-disordered rocksalt ($Li_{1+x}Me_{1-x}O_2$) associated with the formation of percolative network for lithium migration in the host structure.[36]

Galvanostatic charge/discharge curves of Mn^{3+} and Fe^{3+} substituted Li_3NbO_4, *i.e.*, $Li_{1.3}Nb_{0.3}Mn_{0.4}O_2$ and $Li_{1.3}Nb_{0.3}Fe_{0.4}O_2$, are compared in Figure 5. Both samples deliver ~350 mA h g^{-1} of initial charge capacities with a voltage plateau at 4.1–4.3 V. However, a clear difference is noted for discharge. Polarization on discharge is much larger

 © 2019 The Chemical Society of Japan & Wiley-VCH Verlag GmbH & Co. KGaA, Weinheim

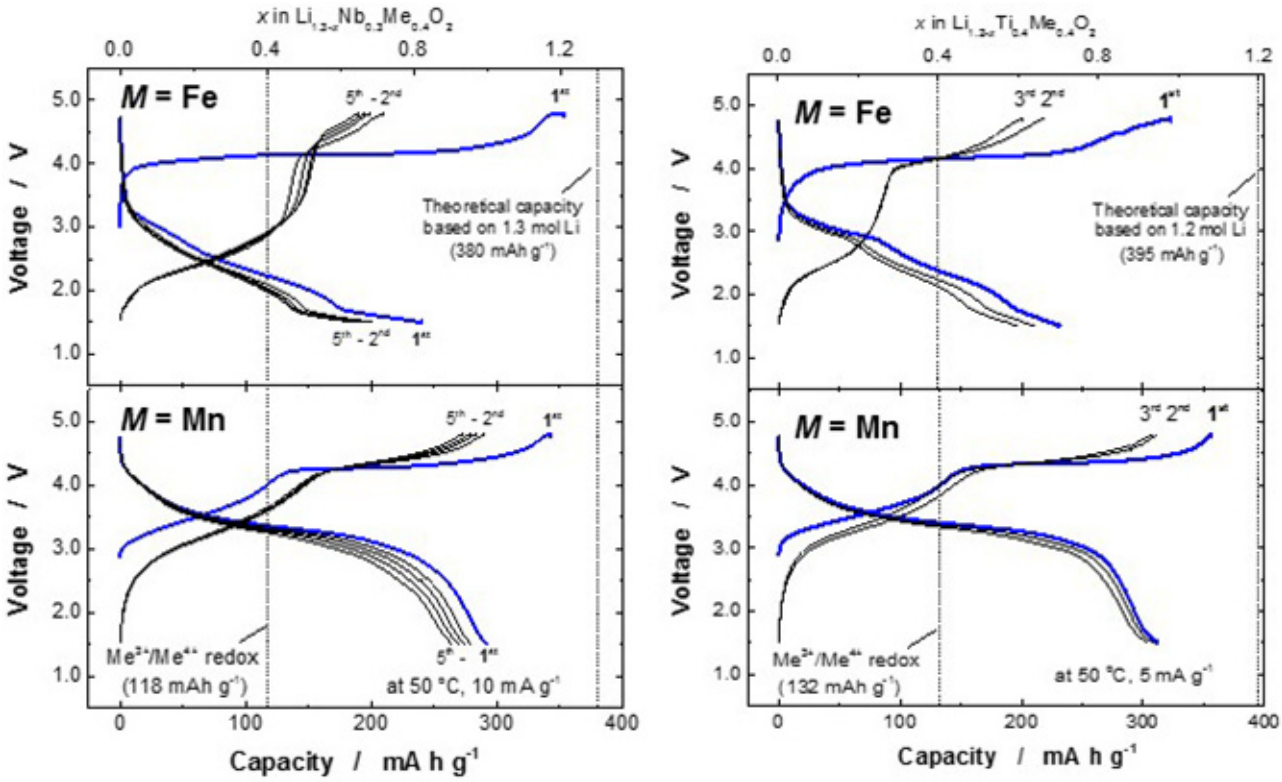

Figure 5. Comparison of charge/discharge curves of $Li_{1.3}Nb_{0.3}M_{0.4}O_2$ and $Li_{1.2}Ti_{0.4}M_{0.4}O_2$ (M=Mn^{3+} and Fe^{3+}). Reprinted with permission from ref 24. Copyright 2017 The Chemical Society of Japan.

for the Fe substituted sample, and the second charge curve is completely different from initial charge. The voltage plateau is observed only for the initial charge. In contrast, profiles of the initial and second charge are similar for the manganese-substituted sample with a slope region (3–4 V) followed by a voltage plateau at 4.3 V. 300 mA h g^{-1} of the reversible capacity is observed for the Mn substituted sample with relatively high voltage on discharge. The discharge capacities observed are much larger than that of the theoretical capacities calculated based on the Mn^{3+}/Mn^{4+} cationic redox. The results suggest that charge compensation is, therefore, realized by anionic redox. Similar to Li_3NbO_4, Li_2TiO_3 is also used as host structure for anionic redox, and charge/discharge curves of $Li_{1.2}Ti_{0.4}M_{0.4}O_2$ (M=Mn^{3+} and Fe^{3+}) are also shown in Figure 5. Niobium- and tatanium-based oxides show similar voltage profiles, and similar reaction mechanisms for both systems are anticipated.

To examine charge compensation mechanisms and the contribution of oxide ions on the charge process, soft X-ray absorption spectroscopy (XAS) was utilized for $Li_{1.2-x}Ti_{0.4}Mn_{0.4}O_2$ (Figure 6).[37] .On charge, no change is observed for Ti L-edge XAS spectra, suggesting that Ti is not responsible for charge compensation. In the slope region (3 to 4 V on charge), shift of Mn L-edge XAS spectra to the higher energy region clearly indicates oxidation of Mn^{3+} to Mn^{4+} while no change is found on charge in the voltage plateau region. In contrast, a new peak appears at 530 eV for O K-edge XAS spectra, and systematic changes as a function of charge capacities are observed during charge in the plateau region. Moreover, this process is reversible, and coming back to its original position after discharge. Such a new peak after charge is also evidenced for Li_2MnO_3-based electrode materials,[38,39] but more clear changes are noted for $Li_{1.3-y}Nb_{0.3}Mn_{0.4}O_2$ and $Li_{1.2-y}Ti_{0.4}Mn_{0.4}O_2$. When it is assumed that charge compensation is realized by anionic redox, formal oxidation states changes from $Li_{1.2}Ti_{0.4}Mn^{3+}{}_{0.4}O_2{}^{2-}$ for the as-prepared sample to $Li_0Ti_{0.4}Mn^{4+}{}_{0.4}O_2{}^{1.6-}$ for the fully charged state. The origin of the new peak has been debatable for a long time.[40] Recently, this peak has been explained by results of the oxidation of π-like bonds between Mn^{4+} ($t_{2g}{}^3$) and O 2p orbitals.[41] After the oxidation of oxygen, holes are energetically stabilized by π-type interaction with Mn^{4+}, which is accompanied by re-hybridization of molecular orbitals, and probably accounts for trend observed in the XAS spectra.

 © 2019 The Chemical Society of Japan & Wiley-VCH Verlag GmbH & Co. KGaA, Weinheim

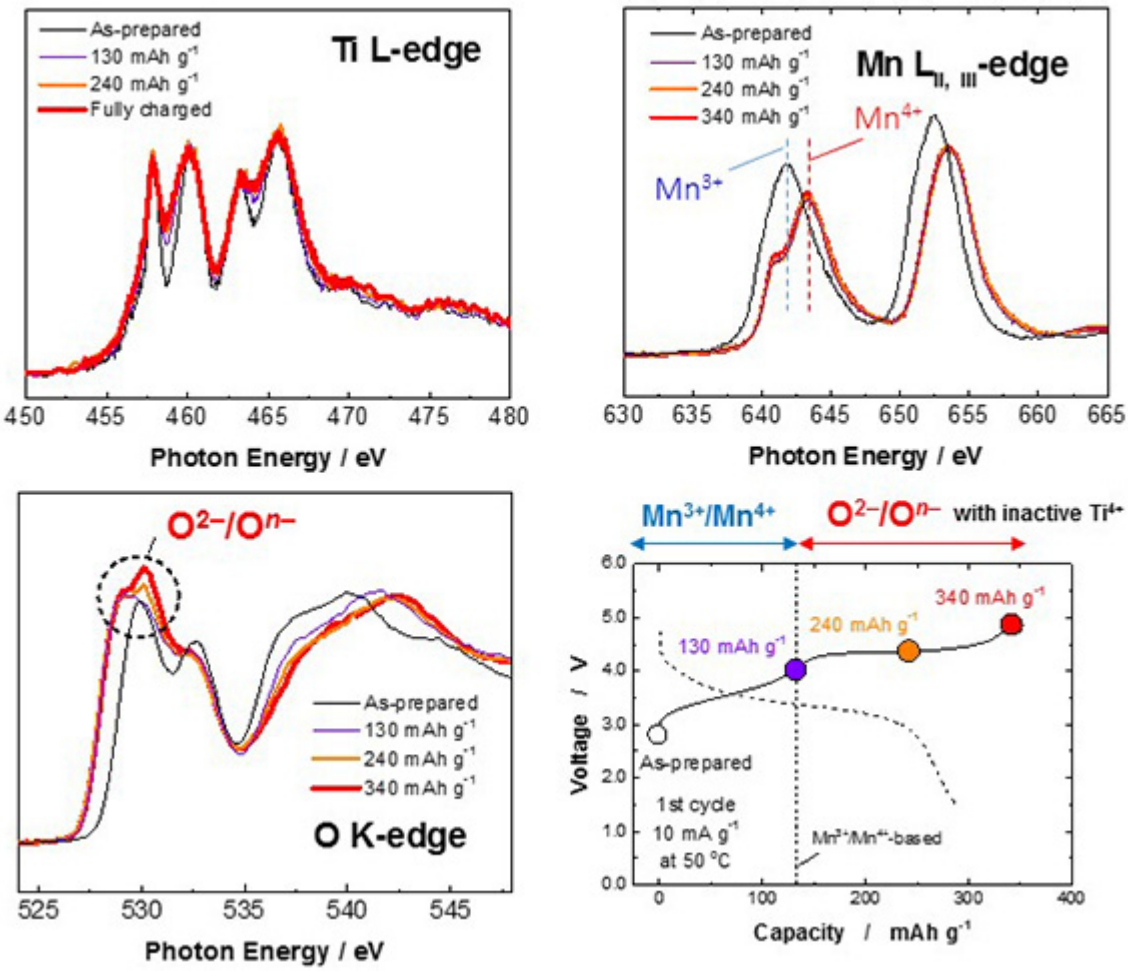

Figure 6. Changes in electronic structures for $Li_{1.2-x}Ti_{0.4}Mn_{0.4}O_2$ on initial charge/discharge; Ti L-edge, Mn L-edge, and O K-edge XAS spectra. The points where XAS spectra have been collected are also shown.

As shown in Figure 5, the iron-substituted samples, $Li_{1.3-y}Nb_{0.3}Fe_{0.4}O_2$ and $Li_{1.2-y}Ti_{0.4}Fe_{0.4}O_2$, show the completely different trend. These results suggest that irreversible phase transition occurs on initial charge. Soft XAS spectra of the Fe-substituted Li_3NbO_4 sample, $Li_{1.3-y}Nb_{0.3}Fe_{0.4}O_2$, on initial charge and discharge are shown in Figure 7. In O K-edge XAS spectra, a new peak at 527.5 eV appears after charge to the point b (120 mA h g^{-1}) in Figure 7. The energy position is clearly different from the manganese systems. Nevertheless, since no change is observed from Fe L-edge XAS spectra, oxygen contributes for the charge compensation process. A similar change was also reported for $Li_{1.19}Ti_{0.38}Fe_{0.42}O_2$.[42] Additionally, this new peak disappears on further charge to 4.8 V. This fact indicates that this intermediate species is energetically unstable, leading to oxygen loss by electrochemical oxidation. Such oxygen loss results in the reconstruction of particle morphology and formation of nanosized particles, and this fact is clearly evidenced in TEM images of Figure 7. After oxygen loss on charge, iron is electrochemically reduced from the trivalent to divalent state on initial discharge, as clearly observed in the Fe L-edge XAS spectra.[37] Instability of anionic redox results in huge polarization observed in Figure 5 for the Fe systems. Similarly, oxygen loss was also found to be the dominative process for $Li_{1.33}Sb_{0.33}Fe_{0.33}O_2$.[43]

For the case of oxides with Fe^{3+}, covalency is relatively high, and therefore, the Fermi level is consisting of both iron and oxygen.[37] After charge, both iron and oxygen are oxidized. Nevertheless, Fe^{4+} is chemically less stable, and therefore oxygen donates electrons to reduce iron ions. As a result, oxygen is further oxidized, leading to oxygen release. In contrast, Mn–O bond has a relatively high ionic character, and Mn^{4+} is chemically more stable. The holes created by oxidation is isolated in the structure (small interaction with

 © 2019 The Chemical Society of Japan & Wiley-VCH Verlag GmbH & Co. KGaA, Weinheim

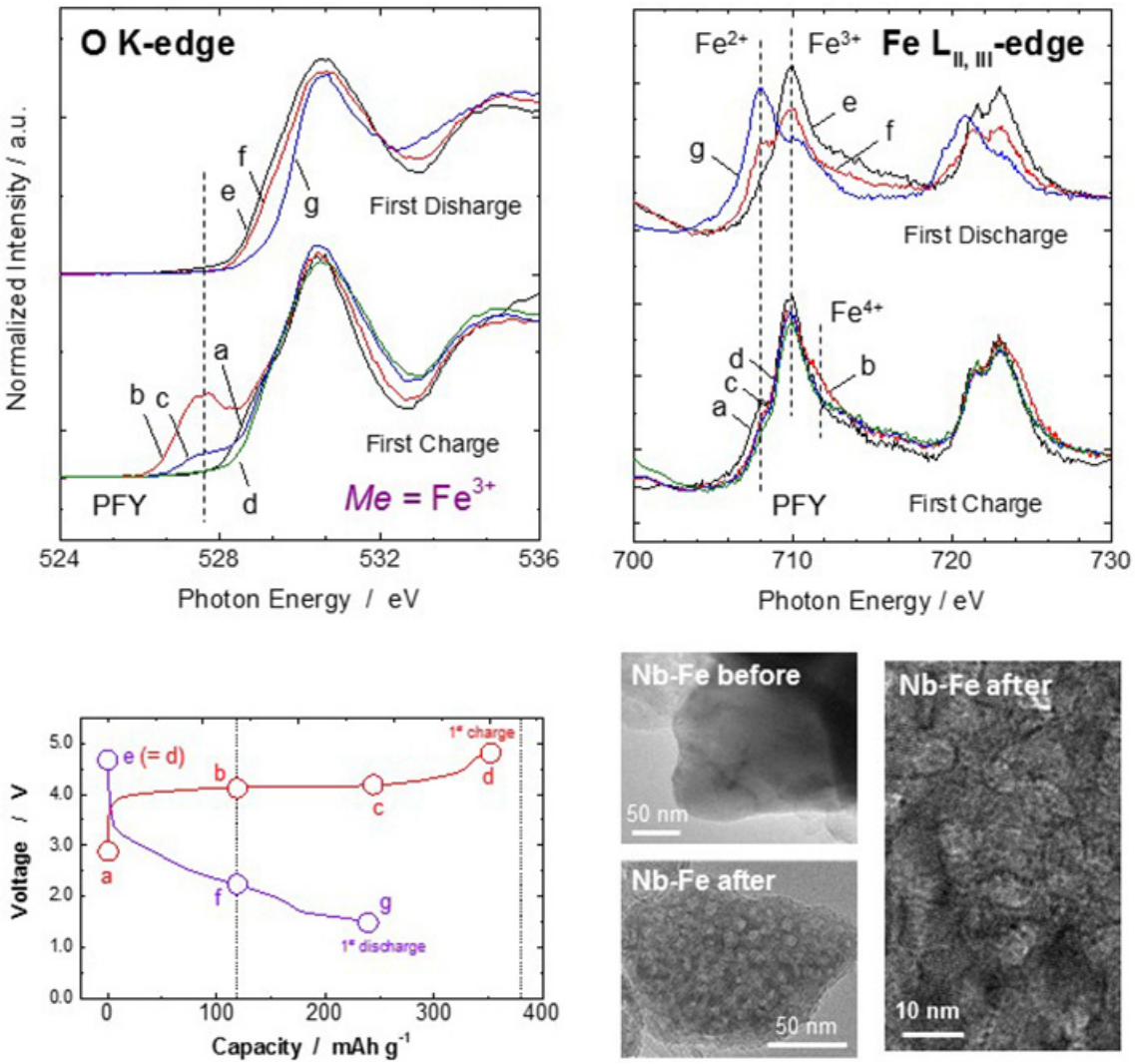

Figure 7. Changes in electronic structures for $Li_{1.3-x}Nb_{0.3}Fe_{0.4}O_2$ on initial charge/discharge; Fe L-edge and O K-edge XAS spectra. The points where XAS spectra have been collected are also plotted. TEM images of $Li_{1.3}Nb_{0.3}Fe_{0.4}O_2$ particles before and after the electrochemical cycle at 50 °C are shown. Oxygen loss for the Fe system results in the formation of nanosized grains in the single particle.

manganese ions), and therefore high reversibility is achieved for the manganese system.

4. Activation of Anionic Redox by Chemical Bonds with High Ionic Characters

Each oxide ion in conventional and stoichiometric layered $LiMO_2$ is coordinated by three transition metal ions and three lithium ions. For the Li-excess layered oxides, Li_2MO_3, oxide ions are coordinated by two transition-metal ions and by four lithium ions. Coordination numbers of lithium ions are increased by Li enrichment. Since a bonding character of Li–O is essentially ionic, the increase in the coordination numbers of lithium ions influences electronic structures of oxide ions. Oxide ions gain more electrons from Li ions, and a net oxidation number approaches its formal oxidation number, two minus. Recently, a rational explanation about such consideration has been provided by the DFT study for the lithium-excess oxides.[44] The lithium-excess oxide contains the Li–O–Li configuration, and the Li–O–Li configuration is essentially unhybridized with transition-metal ions. The energy of this unhybridized state is lower than those of hybridized O 2p states with transition-metal ions, and thus, oxide ions are more easily oxidized for the lithium-excess oxides.

Additionally, Nb^{5+} and Ti^{4+} are also highly ionized ions compared with the late transition metal ions. The mixing

 © 2019 The Chemical Society of Japan & Wiley-VCH Verlag GmbH & Co. KGaA, Weinheim

between metal d orbitals and oxygen 2p orbitals is less pronounced, and thus similar to the lithium enrichment in the structure, the character of oxide ions becomes more ionic. This fact is beneficial to activate anionic redox, leading to lowering the electrochemical potential. Initial charge/discharge profiles of the conventional lithium-excess oxide, $Li_{1.2}Co_{0.13}Ni_{0.13}Mn_{0.54}O_2$,[23] and $Li_{1.2}Ti_{0.4}Mn_{0.4}O_2$[37] in Li cells are compared in Figure 8. Well-defined voltage plateaus are observed for both samples, but voltage related to anionic redox is 0.15 V lower for $Li_{1.2-y}Ti_{0.4}Mn_{0.4}O_2$ than that of $Li_{1.2-x}Co_{0.13}Ni_{0.13}Mn_{0.54}O_2$. Oxide ions are more easily oxidized with a lower electrode potential for $Li_{1.2-y}Ti_{0.4}Mn_{0.4}O_2$. By the presence of Nb^{5+} and Ti^{4+}, anionic redox is more easily accessed when compared with the lithium-excess oxides containing the late transition metal ions. Moreover, for $Li_{1.2-y}Co_{0.13}Ni_{0.13}Mn_{0.54}O_2$, the voltage plateau is lost for the second charge process, as shown in Figure 8 because the partial oxygen loss and structural reconstruction processes cannot be avoided on initial charge.[22,23,45–47] Nevertheless, as pointed out by the recent article,[41] a nature of chemical bonds between oxygen and ions without valence electrons, like Nb^{5+} and Ti^{4+}, is essentially a non-bonding state, and therefore these ions cannot stabilize the redox reaction of oxide ions. Therefore, anionic redox would be stabilized by tetravalent manganese ions through π-type interaction with oxygen.

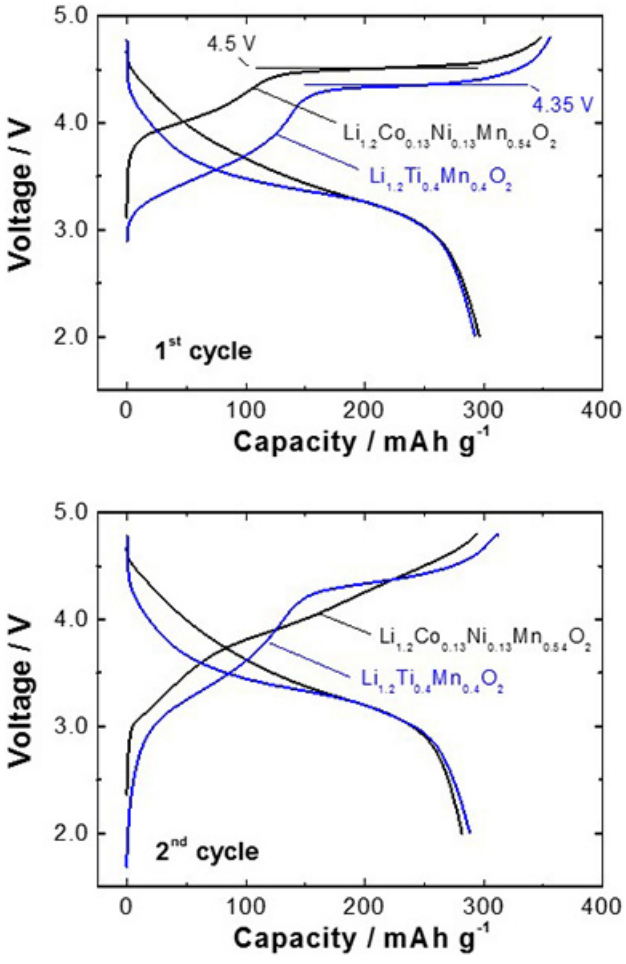

Figure 8. Comparison of 1st and 2nd charge/discharge curves of the conventional Li-excess layered oxide, $Li_{1.2}Ni_{0.13}Ni_{0.13}Mn_{0.54}O_2$, and the cation disordered rocksalt oxide, $Li_{1.2}Ti_{0.4}Mn_{0.4}O_2$, in Li cells. Reprinted with permission from ref 24. Copyright 2017 The Chemical Society of Japan.

5. Li_4MoO_5 as Host Structure of Lithium-Excess Compounds

Li_4MoO_5 has been also studied as a host structure of high-capacity positive electrode materials. To extract lithium ions from Li_4MoO_5, divalent nickel ions are partly substituted for lithium and molybdenum ions based on x Li_4MoO_5–$(1-x)$ NiO binary system with two different rocksalt-type related structures. Synthesis of single-phase samples is achieved in the entire range in this binary system.[48] An XRD pattern of the 1 : 1 mixture of Li_4MoO_5 and NiO, *i.e.*, Li_4NiMoO_6 is shown in Figure 9a. Similarly, Li_4NiMoO_6 is also reformulated as $Li_{4/3}Ni_{1/3}Mo_{1/3}O_2$. The crystal structure of Li_4NiMoO_6 was analyzed by the Rietveld analysis, and it is found that the crystal structure is related to that of Li_5ReO_6. Rhenium ions at 2a sites in Li_5ReO_6 are replaced by molybdenum ions. Additionally, one nickel ion is substituted for one Li ion, resulting in the chemical formula of Li_4NiMoO_6. Nickel and lithium ions are nearly randomly distributed at the same octahedral sites whereas perfect ordering is evidenced for Mo ions as shown in a schematic illustration of the crystal structure in Figure 9a inset.

Electrochemical properties of $Li_{4/3}Ni_{1/3}Mo_{1/3}O_2$ with different cut-off voltages for the charge (oxidation) process are shown in Figure 9b. A large initial charge capacity is observed by charge to 4.8 V, but the polarization as electrode materials is large. Electrode reversibility is improved by lowering the cut-off voltage even though reversible capacity is inevitably lowered. No capacity loss was observed for continuous 15 cycles in the range of 1.5–4.11 V (Figure 9c). When the cut-off voltage is increased from 4.11 to 4.5 V, a discharge (reduction) voltage profile changes. A clear voltage plateau at 2 V appears after charge above 4.5 V, which is clearly different from the voltage profile observed for 4.11 V cycle. To examine the difference in voltage profiles for 4.11 and 4.5 V cycles, *ex-situ* XRD patterns were collected after electrochemical cycles. Diffraction lines related to the Mo ordering, observed in a two theta range of 20–35°, have disappeared after the 4.5 V cycle, and major diffraction lines on the XRD

 © 2019 The Chemical Society of Japan & Wiley-VCH Verlag GmbH & Co. KGaA, Weinheim

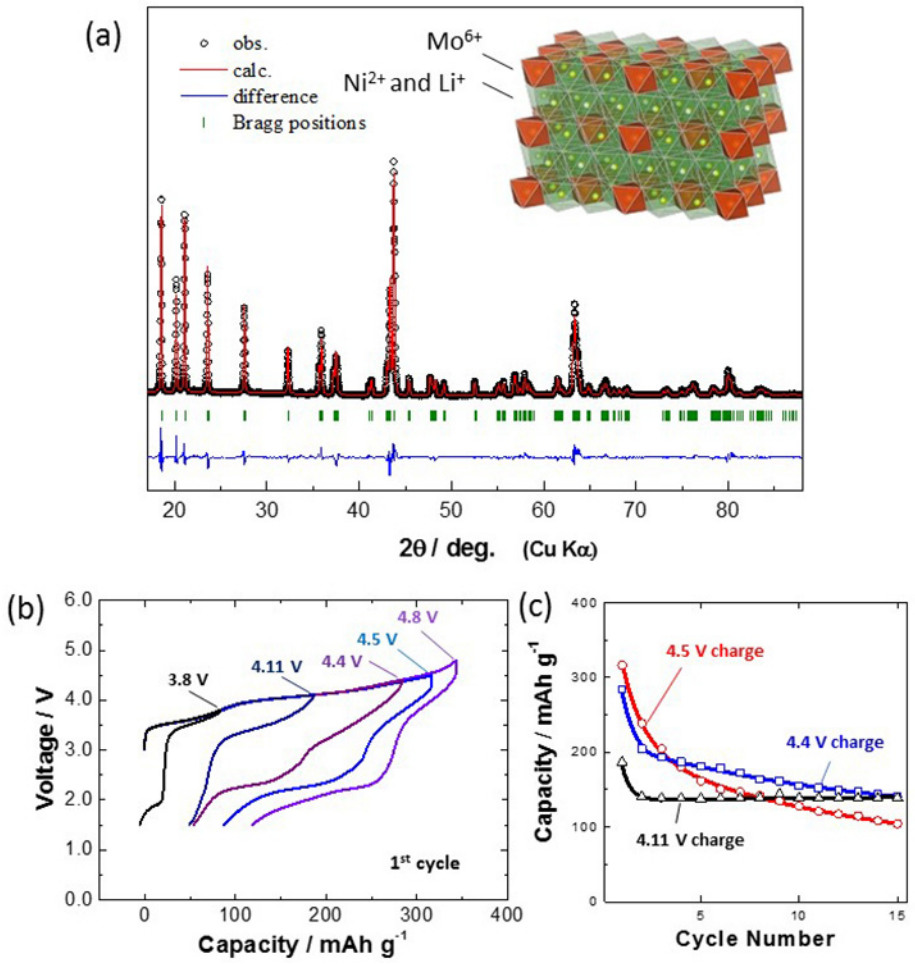

Figure 9. (a) A fitting result by the Rietveld analysis on $Li_{4/3}Ni_{1/3}Mo_{1/3}O_2$, and a schematic illustration of the crystal structure. (b) Galvanostatic oxidation/reduction curves of $Li_{4/3}Ni_{1/3}Mo_{1/3}O_2$ with different cutoff voltages at 10 mA g^{-1}. Charge capacity retention with 4.11, 4.5 and 4.8 V cycles is also compared in (c). Reprinted with permission from ref 48. Copyright 2015 American Chemical Society.

pattern can be assigned as a cation-disordered rocksalt structure.[48] This observation suggests that an irreversible phase transition, at least including Mo migration in the bulk structure, occurs on the 4.5 V cycle. Clear difference is observed on the XRD pattern for the 4.11 V cycle. Diffraction lines related to the Mo ordering are still observed after charge to 4.11 V, suggesting partial oxygen loss on oxidation to above 4.11 V.

Similarly, a binary system, x Li_4MoO_5–$(1-x)$ $LiFeO_2$, is studied as electrode materials for rechargeable lithium batteries.[49] A sample of single phase is obtained at $x=0.5$, and it is found that $Li_{1.42}Mo_{0.29}Fe_{0.29}O_2$ ($x=0.5$) also crystalizes into Li_5ReO_6-type structure. Although an initial charge capacity of $Li_{1.42}Mo_{0.29}Fe_{0.29}O_2$ reaches 350 mA h g^{-1}, irreversible phase transition associated with oxygen loss and molybdenum migration on charge is evidenced by X-ray diffraction and X-ray absorption spectroscopy. The irreversible phase transition inevitably results in large polarization on discharge as electrode materials in Li cells. For late transition metals, such as iron, cobalt and nickel ions, competition of cationic and anionic redox reactions cannot be avoided associated with relatively high covalent natures. The holes created in oxygen are destabilized by charge transfer to cationic species, leading to oxygen loss as the irreversible process.

6. Li_2RuO_3 System; Extremely Reversible Anionic Redox

Although irreversible anionic redox was evidenced for the late 3d-transiton metal ions, an exception is found in Li_2RuO_3 ($Li_{4/3}Ru_{2/3}O_2$). Ruthenium as the 4d-transition metal ion have a much higher covalent nature with oxide ions. However,

 © 2019 The Chemical Society of Japan & Wiley-VCH Verlag GmbH & Co. KGaA, Weinheim

chemical stability of ruthenium ions with higher oxidation states is relatively high when compared with 3d-transition metal ions, and therefore unfavorable charge transfer from oxygen on charge is effectively suppressed. In addition, anionic redox is easily activated associated with high electronic conductivity of Li_2RuO_3,[15] leading to highly reversible anionic redox. Typical charge/discharge curves of Li_2RuO_3 is shown in Figure 10 collected at 50 °C. A reversible capacity of 300 mA h g^{-1}, which corresponds to >90 % of the theoretical capacity, is observed, and surprisingly nearly 2 moles of lithium ions are reversibly extracted from Li_2RuO_3 with the cationic/anionic redox, forming $\square_2RuO_3$ after charge to 4.8 V. Moreover, such electrode properties are obtained from the highly dense particles with large size of ~15 μm as shown in the SEM image of Figure 10. No capacity fading is observed even at 50 °C. Since XRD density is also higher than Ni-based layered materials, both gravimetric/volumetric energy density clearly outperforms stoichiometric layered materials. The only problem is found in material cost of ruthenium as electrode materials.

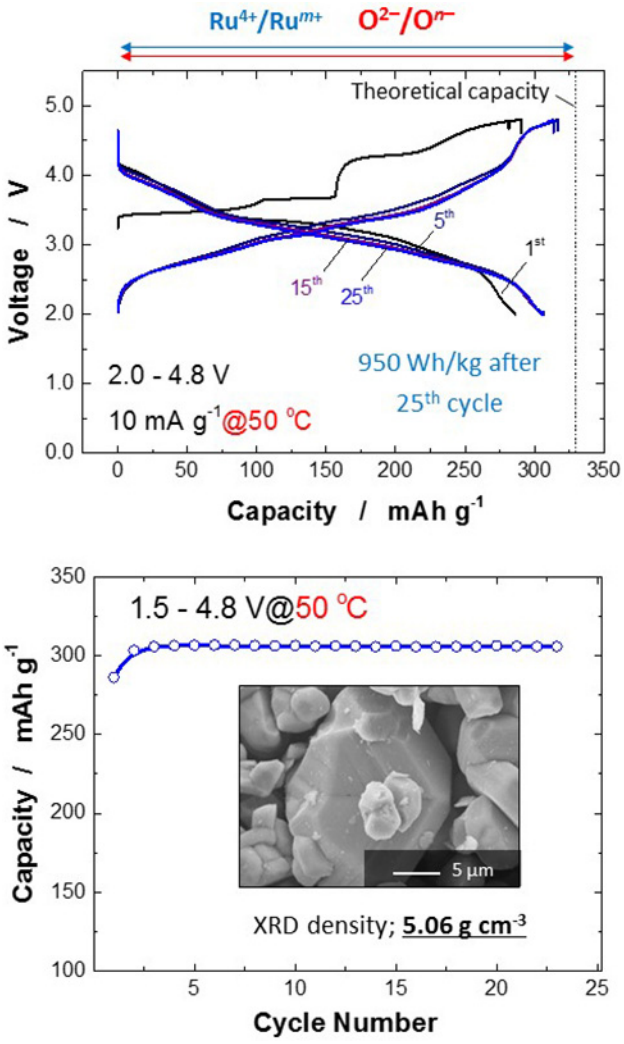

Figure 10. (top) Charge/discharge curves of a Li/Li_2RuO_3 ($Li_{4/3}Ru_{2/3}O_2$) cell at a rate of 10 mA g^{-1} at 50 °C, and (bottom) its capacity retention. No deterioration is evidenced for 25 cycles. Particle morphology of the sample observed by SEM is also shown in the inset.

For the conventional layered oxides, *e.g.*, $LiCoO_2$ and $LiNiO_2$, extraction of 1.0 mol of Li ions from host structures results in the formation of O1 phase[50] (additionally, some stacking faults are noted for Li_xNiO_2[51]), and thus drastic shrinkage of interlayer distances cannot be avoided. This fact is generally used to account for insufficient cyclability for $LiCoO_2$ and $LiNiO_2$ when all Li ions are extracted from oxides. As layered materials, a similar drawback was anticipated for Li_2RuO_3. Nevertheless, no degradation on electrochemical cycles is evidenced in this system. Further studies on reaction mechanisms for the Ru system as model materials of the anionic redox are needed to explain outstanding experimental observation. Similar to Li_2RuO_3, if 2 moles of lithium ions are reversibly extracted from Li_2MO_3 (4/3 moles of lithium ions from $Li_{4/3}M_{2/3}O_2$) with chemistry of 3d-transition metal ions, available reversible capacity possibly exceeds 400 mA h g^{-1} as the electrode materials.

7. Li_3NbO_4-Li$M$$O_2$ System (M=V^{3+} and Mo^{3+}); Pure Cationic Redox

Another group of the lithium-excess compounds is found in vanadium and molybdenum chemistry. Unavoidable competition of cationic/anionic redox often results in oxygen loss for the late 3d-transition metal ions. Since energy of d-electrons for vanadium/molybdenum ions low enough compared with p-electrons of oxygen, such completion of cationic/anionic redox is avoided, and pure cationic redox is, therefore, used as electrode materials. Electrochemical properties of $Li_{1.25}V_{0.25}V_{0.5}O_2$, which is found in Li_3NbO_4–$LiVO_2$ binary system, are shown in Figure 11. In this binary system, both end members crystallize into cation-ordered rocksalt structures, in which lithium, niobium, and vanadium ions are located at distinct octahedral sites. In contrast, $Li_{1.25}V_{0.25}V_{0.5}O_2$ crystallizes into essentially cation-disordered rocksalt structure and cations are located at the same octahedral 4*a* sites.[52] The highest theoretical capacity is expected for the sample of $Li_{1.2}Nb_{0.2}V_{0.6}O_2$ in this binary system based on two-electron redox for V ions (see also Figure 4). However, synthesis of a single phase sample was not successful by conventional calcination.

For $Li_{1.25}V_{0.25}V_{0.5}O_2$, good capacity retention as electrode materials is evidenced, and such high reversibility is advantageous to use two-electron redox reaction of vanadium ions for

 © 2019 The Chemical Society of Japan & Wiley-VCH Verlag GmbH & Co. KGaA, Weinheim

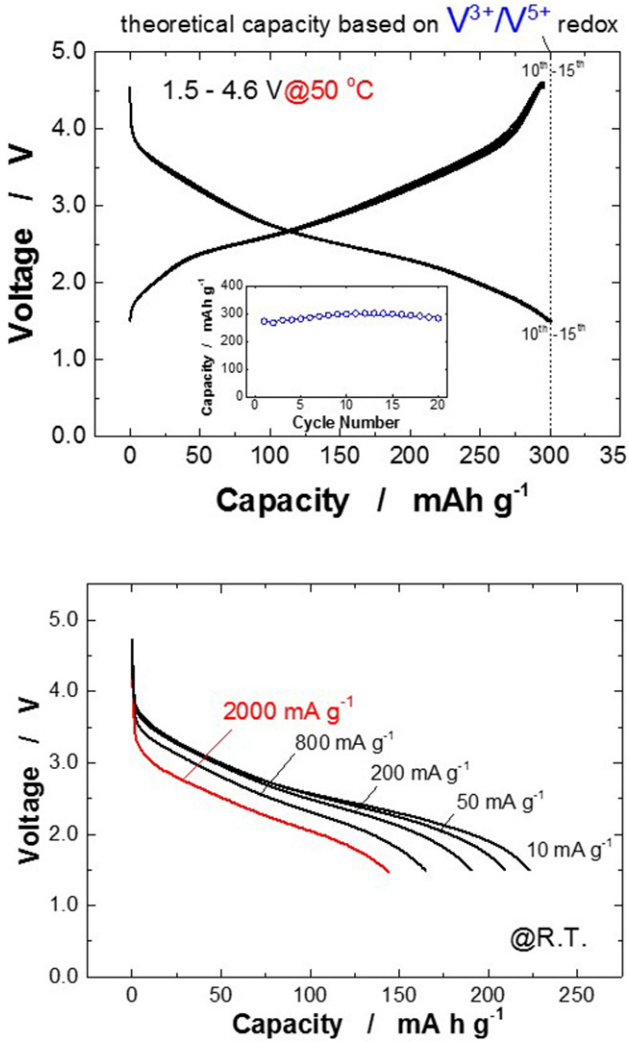

Figure 11. (top) A galvanostatic cycle test of $Li_{1.25}Nb_{0.25}V_{0.5}O_2$ at 10 mA g^{-1} at 50 °C and (bottom) rate capability of $Li_{1.25}Nb_{0.25}V_{0.5}O_2$ Li cells at RT. Reprinted with permission from ref 52. Copyright 2017 American Chemical Society.

battery applications. Moreover, reversible capacity is further enhanced at elevated temperatures. $Li_{1.25}Nb_{0.25}V_{0.5}O_2$ delivers a large capacity of approximately 300 mA h g^{-1} at 50 °C at least for 15 cycles as shown in Figure 11. Energy density available reaches 770 mW h g^{-1} *vs.* Li metal, and this value exceeds those of conventional layered oxides and phosphates. Experimentally observed reversible capacity nearly corresponds to that of the theoretical capacity based on two-electron redox of vanadium ions, indicating that 1.0 mol of Li ions are reversibly extracted from the host structure. Rate-capability of the carbon composite $Li_{1.25}Nb_{0.25}V_{0.5}O_2$ sample is also shown in Figure 11. Discharge capacity observed at a low rate of 10 mA g^{-1} reaches 230 mA h g^{-1} at room temperature, and the sample delivers 150 mA h g^{-1} at a rate of 2000 mA g^{-1}. Inferior rate-capability was expected for the cation-disordered rocksalt phase. However, the sample shows good rate-capability as shown in Figure 11, probably because of good electronic conductivity for the vanadium system.

The theoretical capacity with cation redox is further increased by the use of three-electron redox as shown in Figure 4. Historically, three-electron redox of transition metals is reported for Cr^{3+}/Cr^{6+}, *e.g.*, $Li_{1.2}Cr_{0.4}Mn_{0.4}O_2$.[53] However, chemical compounds containing Cr^{6+} are toxic and restricted in use. Three-electron redox reaction of Mo^{3+}/Mo^{6+} is, therefore, targeted for a new series of electrode materials. Since a conventional layered system, $LiMo^{3+}O_2$, has one mole of Li in the formula unit, only one-electron redox of Mo^{3+}/Mo^{4+} is used.[54] As a proof of concept, Mo^{3+} is diluted in Li_3NbO_4 and tested as a model material to form a binary system with the chemical formula of x $LiMoO_2$–(1−x) Li_3NbO_4. Crystal structures of $LiMoO_2$[54] and Li_3NbO_4[31] are classified as rocksalt-type superstructures, indicating that both oxides consist of a common cubic close-packed (ccp) oxygen lattice, and a difference is found only in cation distribution in octahedral sites. Therefore, similar to other binary systems, the formation of solid solution samples is anticipated. The highest reversible capacity (based on Mo^{3+}/Mo^{6+} redox) is expected when x=0.6 (reformulated as $Li_{9/7}Nb_{2/7}Mo_{3/7}O_2$). If all Li ions are reversibly extracted/re-inserted from/into the crystal lattice with the three-electron redox of Mo, the theoretical capacity reaches 317 mA h g^{-1}. Nevertheless, all our trials to synthesize samples by conventional calcination failed.[55] Phase segregation into Li_3NbO_4 and $LiMoO_2$ has been evidenced, and a narrow solid solution range is anticipated in this binary system. $Li_{9/7}Nb_{2/7}Mo_{3/7}O_2$ was not identified as a thermodynamically stable phase.

Therefore, an alternate route was selected, *i.e.*, synthesis of a metastable phase, and mechanical milling was used for material synthesis.[55] Figure 12a shows X-ray diffraction patterns of the samples before and after the mechanical milling. The diffraction lines of $LiMoO_2$ and $L_{i3}NbO_4$ in a 2θ range of 15–37° are gradually disappeared by mechanical milling, and new peaks are appeared at 38, 42, and 63°, which are assigned as the cation-disordered rocksalt structure. This fact indicates that a mixture of Li_3NbO_4 and $LiMoO_2$ is gradually changed into the cation-disordered rocksalt structure. A single phase sample is successfully obtained after mechanical milling. The heating of the rocksalt sample results in the phase segregation into Li_3NbO_4 and $LiMoO_2$, indicating that this rocksalt phase is a metastable phase.

Electrochemical properties of $Li_{9/7}Nb_{2/7}Mo_{3/7}O_2$ are also shown in Figure 12b. The sample delivers a reversible capacity of $>$280 mA h g^{-1}, which corresponds to approximately 85 % of the theoretical capacity based on the three-electron redox of Mo ions. No degradation is observed for continuous 30 cycles as shown in Figure 12c. Similarly,

 © 2019 The Chemical Society of Japan & Wiley-VCH Verlag GmbH & Co. KGaA, Weinheim

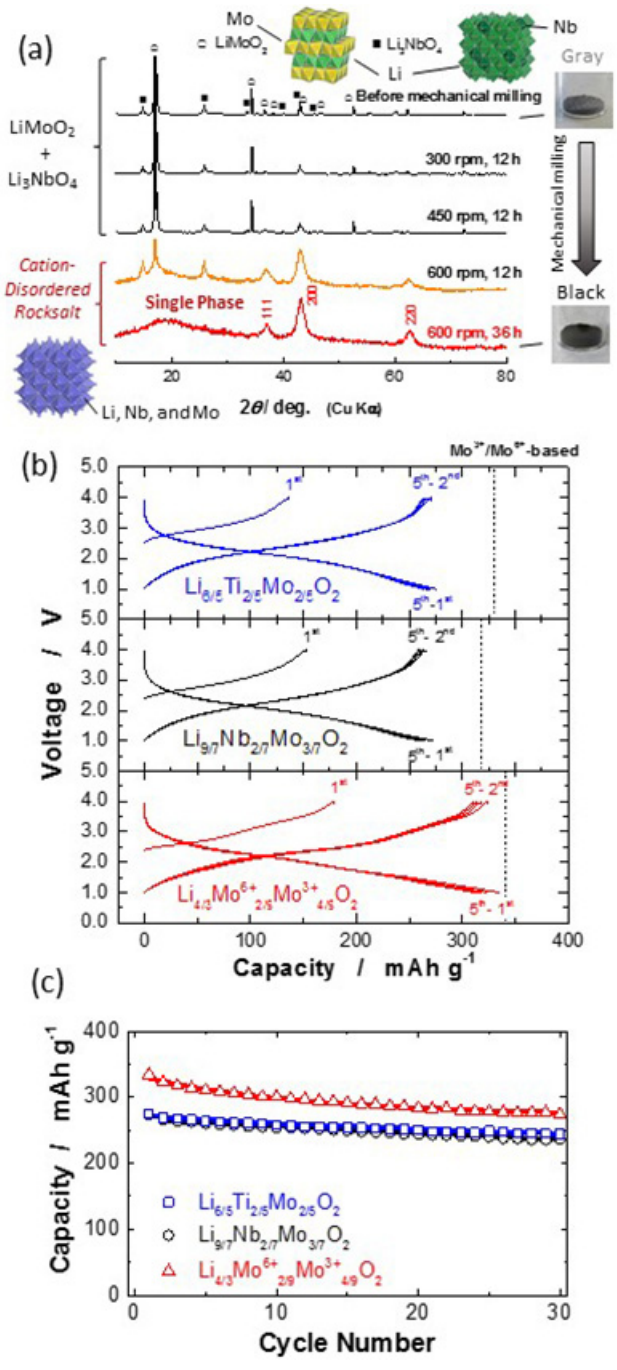

Figure 12. (a) X-ray diffraction patterns of a mixture of Li_3NbO_4 and $LiMoO_2$ before and after the mechanical milling ($Li_{9/7}Nb_{2/7}Mo_{3/7}O_2$). Photographs of powders are also shown. (b) Electrochemical properties of the three different metastable cation-disordered rocksalt phases prepared by the mechanical milling. (c) Capacity retention of the samples in the voltage range of 1.0–4.0 V *vs.* Li at a rate of 10 mA g^{-1}. Reprinted with permission from ref 55. Copyright 2017 American Chemical Society.

Li_2TiO_3 and Li_4MoO_5 are used as starting materials for three-electron redox of molybdenum ions, and solid solution samples with $LiMoO_2$ are obtained by mechanical milling.[55] Reversible capacity exceeds 300 mA h g^{-1} for Li_4MoO_5-$LiMoO_2$ binary system as shown in Figure 12b, and this system, $Li_{4/3}Mo^{6+}{}_{2/9}Mo^{3+}{}_{4/9}O_2$ is reformulated as Li_2MoO_3, in which average oxidation state of Mo is calculated to be "four". Electrochemical properties of Li_2MoO_3 prepared by mechanical milling are much better than that of bulk Li_2MoO_3 prepared by conventional calcination, and reversible capacity observed reaches >90% of theoretical capacity on the basis of Mo^{4+}/Mo^{6+} redox and the lithium content in the structure. Mechanical milling is effective technology to synthesize metastable materials, and electrode performance of samples is drastically improved by nanosizing of materials.

8. Lithium-Excess Metal Oxyfluorides; LiF-Li*M*O$_2$ System

Metal fluorides, such as FeF_3, has been extensively studied as positive electrode materials. A fluoride ion, which is the most electronegative element, effectively increases the electrochemical redox potential, and thus relatively higher operating voltage is achieved for FeF_3 with a redox couple of Fe^{2+}/Fe^{3+}.[56] However, FeF_3 contains no lithium ions in the structure, and therefore fabrication of a full cell with graphite as a negative electrode is impossible. Additionally, FeF_3 crystallizes into a distorted ReO_3-type structure, and a non-close packed structure reduces the volumetric capacity as electrode materials. Lithium-containing close packed structures are, therefore, preferable as positive electrode materials. Similar to layered Li*M*O$_2$, as a fluoride counterpart, Li*M*F$_2$ is considered as potential electrode materials (also see Figure 13). However, in this case, oxidation states of *M* ions are decreased to monovalent, and therefore material designs are restricted to limited chemistry. Moreover, sacrifice of electronic conductivity is also unavoidable for the pure fluoride system. One possible strategy is the use of mixed-anion systems, *i.e.*, metal oxyfluorides, Li*M*OF with divalent transition metal ions. As a lithium-free metal oxyfluoride, FeOF with a rutile structure, which is a distorted close packed structure, is known and is prepared by heating of a mixture of FeF_3 and Fe_2O_3.[57] Lithium ions are reversibly inserted into $Fe^{3+}OF$, ideally forming $LiFe^{2+}OF$. Lithium-containing metal oxyfluorides, $LiM^{2+}OF$, are attractive candidates as potential positive electrode materials. $LiM^{2+}OF$ is also regarded as solid solution of Li*M*O$_2$ and Li*M*F$_2$ as shown in Figure 13. Theoretical capacities of lithium-containing metal oxyfluorides are also shown in Table 2. These oxyfluorides are, unfortunately, not thermodynamically stable, and synthesis is not easy by conventional routes. Nevertheless, it has been reported that synthesis of LiFeOF is possible by mechanical

 © 2019 The Chemical Society of Japan & Wiley-VCH Verlag GmbH & Co. KGaA, Weinheim

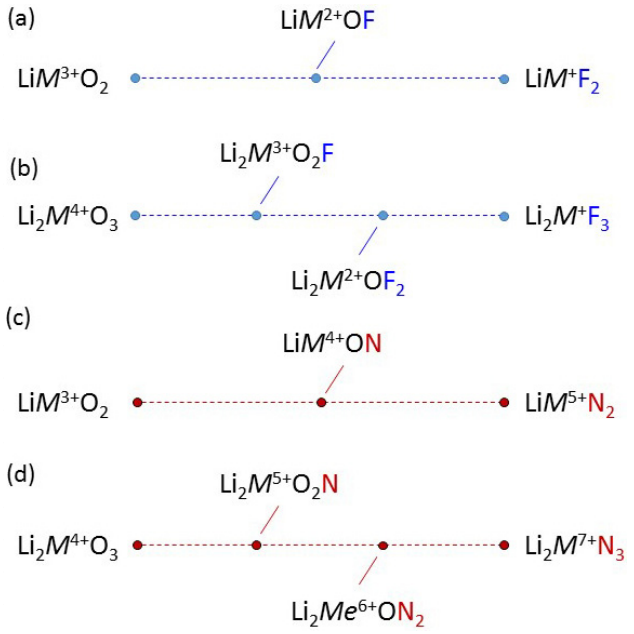

Figure 13. A materials design concept for stoichiometric/lithium-excess fluorides, nitrides, oxyfluorides, and oxynitrides with rocksalt-related structures. See the text for more details.

Table 2. Comparison of theoretical capacity for rocksalt-related metal oxyfluorides and oxynitrides. M = Mn is assumed for the calculation.

LiMOF	Li$_2M$O$_2$F	LiMON	Li$_2M$O$_2$N
277 mAh g^{-1}	447 mAh g^{-1}	292 mAh g^{-1}	467 mAh g^{-1}

milling,[58] and nearly one mole of lithium ions are reversibly extracted from the crystal lattice with Fe^{2+}/Fe^{3+} redox. Similarly, lithium-excess metal oxyfluorides are obtained by mechanical milling. Li_2VO_2F has been reported as a first lithium-excess metal oxyfluoride,[59] and Li_2MO_2F is also found in a phase diagram between Li_2MO_3 and Li_2MF_3 (Figure 13). Li_2VO_2F ($Li_{1.33}V_{0.67}O_{1.33}F_{0.67}$), delivers large reversible capacity of 350 mAh g^{-1} in Li cells on the basis of V^{3+}/V^{5+} two-electron redox. However, in general, solubility of fluorides into carbonate solvents is higher than that of oxides,[56] and therefore improvement of cyclability is needed for battery applications.

Recently, our group has extended the concept of three-electron redox of Mo^{3+}/Mo^{6+} to the oxyfluoride, and relatively low electrochemical potential of Mo redox (2–3 V vs. Li) is effectively increased by partial substitution of fluoride ions for oxide ions.[60] Lithium molybdenum oxyfluorides were prepared from a mixture of $LiMoO_2$ and LiF. Crystal structures of $LiMoO_2$[54] and LiF are also classified as rocksalt-type (super)structures consisting of a common cubic close-packed (ccp) anion lattice, and a difference is found only in cation distribution in octahedral sites. Therefore, the formation of solid solution samples ($Li_{1+x}MoO_2F_x$ or $Li_{1+x}Mo_{1-x}O_{2-2x}F_{2x}$) is anticipated, and the highest reversible capacity (based on the Mo^{3+}/Mo^{6+} redox) is expected for $Li_3MoO_2F_2$ ($x=2$). Indeed, a uniform distribution of Mo/O/F is clearly noted by EDX mapping after mechanical milling as shown in Figure 14, and the formation of a single phase sample with low crystallinity is further confirmed by XRD.[60] If all lithium ions are reversibly extracted from the crystal lattice with the three-electron redox of Mo, the theoretical capacity reaches 430 mAh g^{-1}. $Li_{1+x}MoO_2F_x$ samples with different compositions deliver large reversible capacities of over 250 mAh g^{-1} in lithium cells. The highest reversible capacity is obtained for $x=1$, Li_2MoO_2F, and the sample delivers more than 300 mAh g^{-1} (Figure 14). Moreover, operating voltage is increased in comparison to the non-fluorine substituted sample, which is also prepared by mechanical milling, as shown in Figure 14. Energy density observed

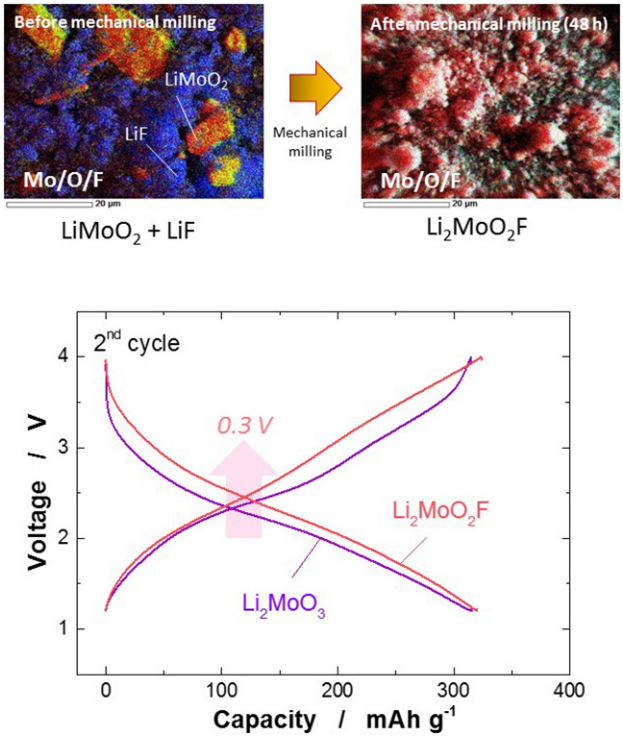

Figure 14. (top) SEM/EDX images of a mixture of $LiMoO_2$ and LiF ($x=2$ in xLiF–$LiMoO_2$) before/after the mechanical milling. The mixture gradually changes into cation disordered rocksalt-type phase by mechanical milling. Uniform contrast for Mo, O, and F is clearly evidenced for the EDX map after mechanical milling. (bottom) Comparison of charge/discharge curves of Li_2MoO_3[55] and Li_2MoO_2F ($x=1$ in xLiF–$LiMoO_2$) prepared by mechanical milling. Operating voltage is increased by fluorine-substitution. Reprinted with permission from ref 60. Copyright 2017 Elsevier B.V..

 © 2019 The Chemical Society of Japan & Wiley-VCH Verlag GmbH & Co. KGaA, Weinheim

reaches 750 mWh g^{-1} based on Li metal, and is comparable to layered positive electrode materials with nickel and cobalt. Although redox potential of molybdenum ions is relatively low as positive electrode materials, operating voltage is effectively increased by LiF substitution through an inductive effect[61] by electronegative fluoride ions. Nevertheless, the reversible capacities decrease by further enrichment of fluoride ions. The observed reversible capacity for $x=2$ is limited to only 60% of the theoretical capacity. This observation is expected to originate from the inferior electronic conductivity for the fluorine-rich phases.

Electrode performance of other lithium-excess metal oxyfluorides, Li_2VO_2F[59] and Li_2CrO_2F,[62] collected at room temperature is also compared with Li_2MoO_2F in Figure 15. Both samples were similarly prepared by ball milling. The vanadium system shows slightly higher operating voltage compared with the molybdenum-system. Moreover, operating voltage is further increased for the chromium-system, but polarization on discharge is larger compared with vanadium-/molybdenum-system. Irreversible migration of Cr ions would be responsible for the polarization as observed in a lithium-excess layered oxide containing Cr ions.[63] Very recently, a manganese system, Li_2MnO_2F, has been already reported. The sample delivers a reversible capacity of nearly 300 mA h g^{-1}, which partly originates from the anionic redox reaction.[64] In addition, it has been reported that $Li_2Mn_{2/3}Nb_{1/3}O_2F$ also delivers a reversible capacity of approximately 300 mA h g^{-1} in lithium cells on the basis of Mn^{2+}/Mn^{4+} redox coupled with partial anionic redox.[65]

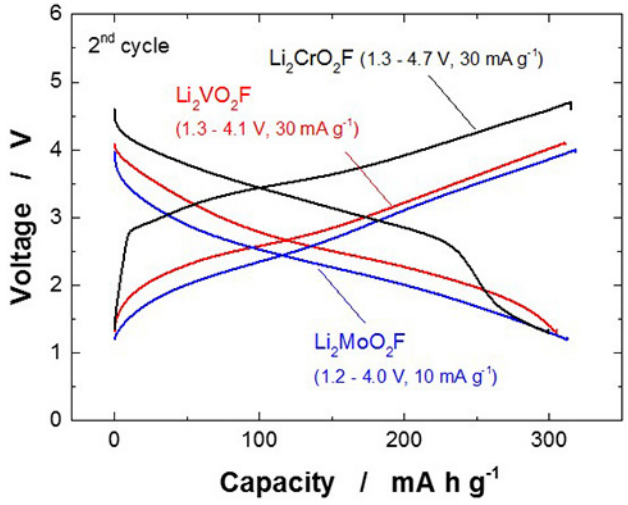

Figure 15. Comparison of charge/discharge curves of lithium-excess metal oxyfluorides; Li_2VO_2F, Li_2CrO_2F, and Li_2MoO_2F.

Theoretical capacities, experimentally observed reversible capacities, and average operating voltage of lithium-excess rocksalt oxides/oxyfluorides shown in this manuscript are plotted and compared in Figure 16. As shown in this manuscript, now, reversible capacities of 300 mA h g^{-1} are realized for many chemistries with cationic/anionic redox. For the case of ruthenium system, Li_2RuO_3, the observed reversible capacity is very close to that of the theoretical capacity (also see Figure 10). In contrast, for the manganese-based oxides/oxyfluorides, observed reversible capacities are clearly smaller than those of theoretical capacities, and observed reversible capacities are possibly further increased by further optimization of electrode materials. Average operating voltage of vanadium-/molybdenum-based electrode materials is relatively low (*ca.* 2.5 V *vs.* lithium metal) as positive electrode materials, but high safety with moderate energy density is anticipated. In contrast, nickel-based system, high average operating voltage is attractive even though observed reversible capacity is currently limited. If reversibility of anionic redox is improved for the nickel-based system, available energy density would be significantly improved.

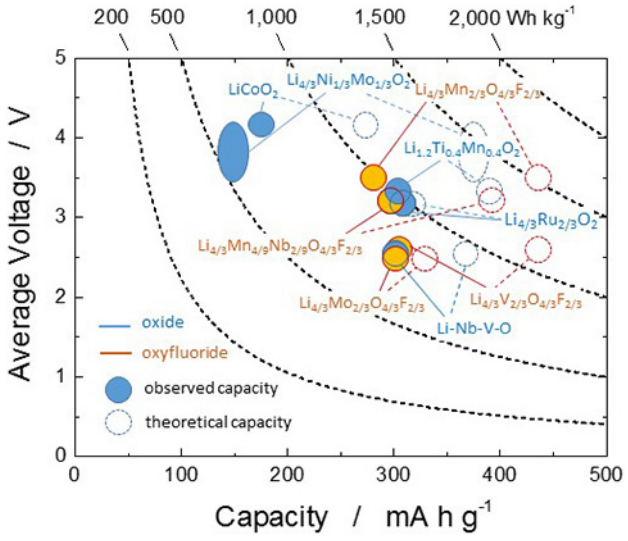

Figure 16. Comparison of observed reversible capacity (mA h g^{-1}), average operating voltage (V), and calculated energy density (Wh kg^{-1}) based on metallic lithium for different lithium-excess metal oxides and oxyflurodies. Theoretical capacity on the basis of lithium contents in the structure is also shown.

Similar to the oxyfluorides, the concept of is extended to a nitride system as shown in Figure 13, but the requirements of metals with high oxidation states results in the difficulty of material designs with rocksalt-related structures. Among expected compounds shown in Figure 13, $LiMoN_2$ with layered structure was synthesized and tested as electrode

 © 2019 The Chemical Society of Japan & Wiley-VCH Verlag GmbH & Co. KGaA, Weinheim

materials.[66] In contrast to fluorine-substitution, $LiMoN_2$ has significantly low resistivity, and nitride-substitution is an effective strategy to increase the electronic conductivity as electrode materials. Although $LiMoN_2$ crystallizes into a non-close packed structure (molybdenum ions are located at prismatic sites), lithium ions are indeed extracted by electrochemical oxidation. Lithium ions are also inserted into a metal oxynitride, NbON with a baddeleyite-type (ZrO_2) structure,[67] and NbON is used as potential negative electrode materials. Since fluoride/nitride ions have unique functionality compared with oxide ions, such mixed anion systems potentially open a new direction to design electrode materials in the future.

9. Anionic Redox Reaction for Rechargeable Sodium Batteries

The use of redox reactions of oxide ions is not limited to the Li system, and is easily extended to the system with different mobile ions, and the application of anion redox has been extended for sodium insertion materials. Na_2MnO_3, which is a hypothetical Na counterpart of Li_2MnO_3, is considered to be the host structure of high-capacity sodium insertion materials. Nevertheless, synthesis of Na_2MnO_3 ($Na(Na_{1/3}Mn_{2/3})O_2$) as an isostructural phase with Li_2MnO_3 is difficult by conventional synthesis routes associated with a large gap in size of Na^+ and Mn^{4+} ions. Instead, the use of $Na(Li_{1/3}Mn_{2/3})O_2$ has been proposed in the literature.[68] Although synthesis of the stoichiometric phase is difficult, a non-stoichiometric Na-deficient phase, $Na_{5/6}(Li_{1/4}Mn_{3/4})O_2$, has been successfully obtained.[68] Similar to Li_2MnO_3-based electrode materials, a well-defined voltage plateau is observed for $Na_{5/6}(Li_{1/4}Mn_{3/4})O_2$ in the Na cell. Partial oxygen loss results in the disappearance of the plateau from the second cycle, but the sample delivers a large reversible capacity of 200 mA h g^{-1} in the Na cell.[68] Similarly, a large reversible capacity was reported for $Na_{0.6}Li_{0.6}Ni_{0.25}Mn_{0.75}O_y$,[69] and such large capacity cannot be obtained without the contribution of anion redox. A reversible voltage plateau at 4.2 V vs. Na metal (4.5 V vs. Li metal), presumably associated with oxide ion redox, has been also reported for $Na_{0.6}(Li_{0.2}Mn_{0.8})O_2$.[70] Mg ions are substituted for Li ions in transition metal layers. $Na_{2/3}(Mg_{0.28}Mn_{0.72})O_2$ delivers large reversible capacity of more than 200 mA h g^{-1},[71] and the contribution of reversible anionic redox has been reported.

Recently, the reversible redox reaction of oxide ions has been evidenced for Ru-based layered compounds.[72,73] Similar to Li_2RuO_3, Na_2RuO_3 crystallizes into the α-$NaFeO_2$-type layered structure. Two layered polymorphs, in-plane Na/Ru ordered and disordered phases, exist and the anionic redox is activated only for the ordered phase.[72] The origin of activation has been proposed to be the formation and stabilization of the intermediate phase, ilmenite-type $NaRuO_3$, associated with glide of layers. A similar phase is also found in the Li counterpart.[15] This process involves the phase transition from ccp to hexagonal closed packing (hcp) for the oxygen arrangement. It has been also proposed that large distortion of RuO_6 octahedra for the ilmenite phase triggers the formation of O–O sigma antibonding state, and thus the anion redox is also activated.[72]

Similar to Li_3NbO_4, Na_3NbO_4 has been also studied as a model host structure for high-capacity positive electrodes. Na and Nb ions are located at octahedral sites in a cubic-close packed (ccp) lattice of oxide ions, and clusters consisting of four Nb ions are surrounded by sodium ions (Figure 17a). If all Na ions are extracted/re-inserted from/into the crystal

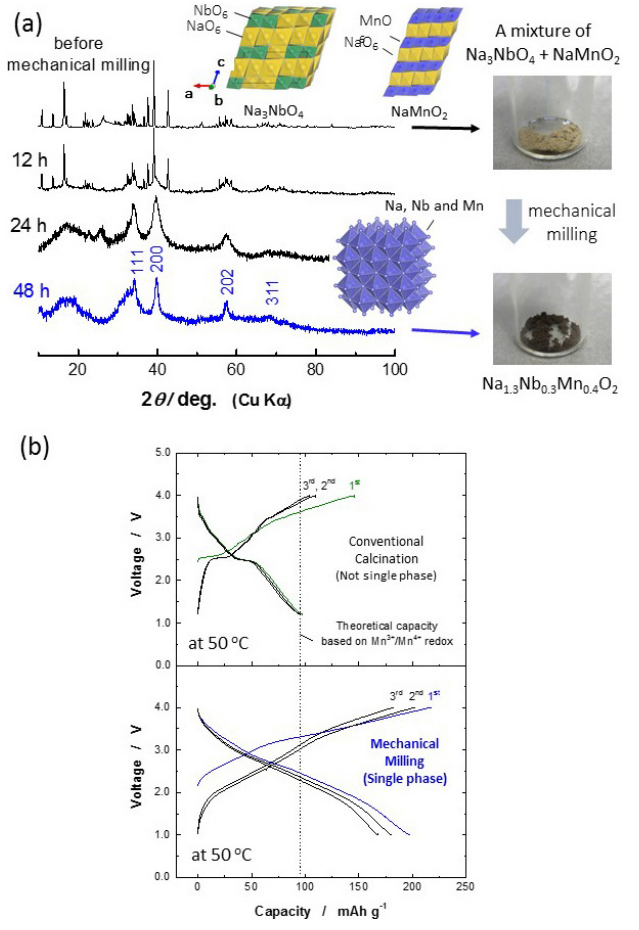

Figure 17. (top) Synthesis of $Na_{1.3}Nb_{0.3}Mn_{0.4}O_2$ by mechanical milling; (a) X-ray diffraction patterns of a mixture of Na_3NbO_4 and $NaMnO_2$ before/after the mechanical milling. Photographs of powders are also shown. (bottom) Electrochemical properties of $Na_{1.3}Nb_{0.3}Mn_{0.4}O_2$ at a rate of 10 mA g^{-1}; comparison of electrode performance for the sample prepared by the conventional calcination and mechanical milling. Reprinted with permission from ref 74. Copyright 2017 American Chemical Society.

 © 2019 The Chemical Society of Japan & Wiley-VCH Verlag GmbH & Co. KGaA, Weinheim

lattice, the theoretical capacity reaches 356 mA h g^{-1}. A binary system, Na_3NbO_4–$NaMnO_2$ has been examined as possible high-capacity positive electrode materials for sodium battery applications.[74] However, synthesis of samples by conventional calcination is impossible. Phase segregation into Na_3NbO_4 and $NaMnO_2$ was evidenced, and a narrow solid solution range is expected in this binary system. Therefore, similar to other systems, mechanical milling was used to synthesize metastable phases. Figure 17a shows X-ray diffraction patterns of a mixture of Na_3NbO_4 and $NaMnO_2$ before and after the mechanical milling. The mixture gradually changes into a cation-disordered rocksalt-type structure. Color of powders also changes into black after the mechanical milling. Although the size of Na^+ is much larger than those of Nb^{5+} and Mn^{3+}, all cations are located at the same octahedral sites in the ccp lattice. The sample segregates into a mixture of Na_3NbO_4 and $NaMnO_2$ after heating, indicating that this phase is a metastable phase. From the scientific point of view, such a metastable phase is quite interesting and important as insertion materials. Nevertheless, from the practical point of view, the difficulty in the synthesis of these materials hinder the use for battery applications because of the cost limitation. Therefore, the research progress on synthesis of metastable phases, possibly the development of a continuous flow process with low cost, is needed to solve this practical problem in the future.

Electrochemical properties of the samples prepared by the conventional calcination and mechanical milling are compared in Figure 17b. A theoretical capacity reaches 311 mA h g^{-1} when all Na ions are extracted from $Na_{1.3}Nb_{0.3}Mn_{0.4}O_2$. However, the sample prepared by the conventional calcination delivers only 95 mA h g^{-1}, nearly corresponding to the theoretical capacity based on the Mn^{3+}/Mn^{4+} redox. This result indicates that O^{2-} redox is not activated. In contrast, the sample obtained by the mechanical milling delivers a large reversible capacity of approximately 200 mA h g^{-1} at 50 °C, indicating that anionic redox is effectively activated for the sodium-excess condition. Electrochemical voltage of the sample increases almost linearly with two different slope angles, which change at 3.2 V. The potential profile of the sample is similar to the case of Li_2MnO_3-based electrode materials. However, a clear voltage plateau as observed for $Li_{1.3}Nb_{0.3}Mn_{0.4}O_2$[31,37] is not found for the Na counterpart. Moreover, cyclability of the sample in the Na cell is not acceptable for battery applications. Reversibility is completely lost after only 20 cycles.[74] Metastable phases prepared by mechanical milling consists of nanosize particles with low crystallinity, and therefore anionic redox is destabilized compared with submicrometer-sized particles. Indeed, reversibility as electrode materials is significantly improved for nanosize $NaMnO_2$ with the cation-disordered rocksalt structure prepared by mechanical milling.[75]

10. Conclusions and Future Perspectives

Lithium-excess compounds with rocksalt-related structures are attractive as positive electrode materials for rechargeable lithium/sodium batteries. Higher lithium (sodium) contents with fewer transition-metal ions in framework structures effectively increases theoretical capacities as positive electrode materials. A wide variety of material designs is possible with different chemistry on the basis of both cationic/anionic redox. In the past several years, many new positive electrode materials appeared. Moreover, the concept of the anion redox reaction, not only for the oxide system is extended to the sulfide system.[76] In addition, these concepts would be extended non-rocksalt system, *e.g.*, $Li_4Mn_2O_5$[77] and Li_2O system.[78–80] Experimental and theoretical understandings of cationic/anionic redox are also further accelerated from the research progress on oxygen electrocatalysts as another important anionic redox system,[81] and a possible synergy between battery materials and electrocatalysts is anticipated.[82] Nevertheless, cyclability of anionic redox as electrode material is currently not enough for practical battery applications. The surface of electrode materials can be chemically reactive after the activation of anionic redox, probably leading to unfavorable side reactions with electrolyte and growth of impedance on electrochemical cycles. In contrast, pure cationic redox system, and the exception of Li_2RuO_3, shows much better cyclability, and will be used for battery applications soon. Further studies of degradation mechanisms are, therefore, encouraged to solve the cyclability problem of anionic redox. Indeed, stabilization of anionic redox has been recently proposed by fluorination.[83] Coordination numbers of transition metal ions with d-electrons to oxygen also significantly influence the reversibility of anionic redox through σ-type interaction.[84] Further understanding results in the development of high energy electrode materials with highly reversible anionic redox in the future.

Acknowledgments

The author acknowledges M. Nakayama at Nagoya Institute of Technology, T. Ohta at Ritsumeikan University for the collaboration and fruitful discussions. The author acknowledges research funding from JSPS KAKENHI Grant Number 18H02076 and MEXT program "Elements Strategy Initiative to Form Core Research Center", MEXT; Ministry of Education Culture, Sports, Science and Technology, Japan.

 © 2019 The Chemical Society of Japan & Wiley-VCH Verlag GmbH & Co. KGaA, Weinheim

References

[1] B. Dunn, H. Kamath, J.-M. Tarascon, *Science* **2011**, *334*, 928–935.
[2] T. Ohzuku, A. Ueda, *Solid State Ionics* **1994**, *69*, 201–211.
[3] K. Mizushima, P. C. Jones, P. J. Wiseman, J. B. Goodenough, *Mater. Res. Bull.* **1980**, *15*, 783–789.
[4] A. Ueda, T. Ohzuku, *J. Electrochem. Soc.* **1994**, *141*, 2010–2014.
[5] H. Arai, S. Okada, Y. Sakurai, J.-i. Yamaki, *Solid State Ionics* **1998**, *109*, 295–302.
[6] M. Guilmard, L. Croguennec, D. Denux, C. Delmas, *Chem. Mater.* **2003**, *15*, 4476–4483.
[7] M. Guilmard, L. Croguennec, C. Delmas, *Chem. Mater.* **2003**, *15*, 4484–4493.
[8] Y. Makimura, T. Sasaki, T. Nonaka, Y. F. Nishimura, T. Uyama, C. Okuda, Y. Itou, Y. Takeuchi, *J. Mater. Chem. A* **2016**, *4*, 8350–8358.
[9] T. Ohzuku, Y. Makimura, *Chem. Lett.* **2001**, 642–643.
[10] N. Yabuuchi, T. Ohzuku, *J. Power Sources* **2003**, *119*, 171–174.
[11] Z. H. Lu, D. D. MacNeil, J. R. Dahn, *Electrochem. Solid-State Lett.* **2001**, *4*, A200–A203.
[12] H.-J. Noh, S. Youn, C. S. Yoon, Y.-K. Sun, *J. Power Sources* **2013**, *233*, 121–130.
[13] J. N. Reimers, J. R. Dahn, *J. Electrochem. Soc.* **1992**, *139*, 2091–2097.
[14] G. C. Mather, C. Dussarrat, J. Etourneau, A. R. West, *J. Mater. Chem.* **2000**, *10*, 2219–2230.
[15] H. Kobayashi, R. Kanno, Y. Kawamoto, M. Tabuchi, O. Nakamura, M. Takano, *Solid State Ionics* **1995**, *82*, 25–31.
[16] Z. H. Lu, L. Y. Beaulieu, R. A. Donaberger, C. L. Thomas, J. R. Dahn, *J. Electrochem. Soc.* **2002**, *149*, A778–A791.
[17] Z. H. Lu, J. R. Dahn, *J. Electrochem. Soc.* **2002**, *149*, A815–A822.
[18] A. D. Robertson, P. G. Bruce, *Chem. Mater.* **2003**, *15*, 1984–1992.
[19] C. S. Johnson, J. S. Kim, C. Lefief, N. Li, J. T. Vaughey, M. M. Thackeray, *Electrochem. Commun.* **2004**, *6*, 1085–1091.
[20] D. Y. W. Yu, K. Yanagida, Y. Kato, H. Nakamura, *J. Electrochem. Soc.* **2009**, *156*, A417–A424.
[21] M. Sathiya, K. Ramesha, G. Rousse, D. Foix, D. Gonbeau, A. S. Prakash, M. L. Doublet, K. Hemalatha, J. M. Tarascon, *Chem. Mater.* **2013**, *25*, 1121–1131.
[22] N. Yabuuchi, K. Yoshii, S.-T. Myung, I. Nakai, S. Komaba, *J. Am. Chem. Soc.* **2011**, *133*, 4404–4419.
[23] N. Yabuuchi, K. Kubota, Y. Aoki, S. Komaba, *J. Phys. Chem. C* **2016**, *120*, 875–885.
[24] N. Yabuuchi, *Chem. Lett.* **2017**, *46*, 412–422 10.1246/cl.161044.
[25] L. Blandeau, G. Ouvrard, Y. Calage, R. Brec, J. Rouxel, *J. Phys. C* **1987**, *20*, 4271.
[26] A. E. Bocquet, A. Fujimori, T. Mizokawa, T. Saitoh, H. Namatame, S. Suga, N. Kimizuka, Y. Takeda, M. Takano, *Phys. Rev. B* **1992**, *45*, 1561–1570.
[27] J. M. Tarascon, G. Vaughan, Y. Chabre, L. Seguin, M. Anne, P. Strobel, G. Amatucci, *J. Solid State Chem.* **1999**, *147*, 410–420.
[28] K. Ukei, H. Suzuki, T. Shishido, T. Fukuda, *Acta Crystallogr. Sect. C* **1994**, *50*, 655–656.
[29] R. Hoffmann, R. Hoppe, *Z. Anorg. Allg. Chem.* **1989**, *573*, 157–169.
[30] T. Betz, R. Hoppe, *Z. Anorg. Allg. Chem.* **1984**, *512*, 19–33.
[31] N. Yabuuchi, M. Takeuchi, M. Nakayama, H. Shiiba, M. Ogawa, K. Nakayama, T. Ohta, D. Endo, T. Ozaki, T. Inamasu, K. Sato, S. Komaba, *Proc. Natl. Acad. Sci. USA* **2015**, *112*, 7650–7655.
[32] N. Yabuuchi, M. Takeuchi, S. Komaba, S. Ichikawa, T. Ozaki, T. Inamasu, *Chem. Commun.* **2016**, *52*, 2051–2054.
[33] L. A. de Picciotto, M. M. Thackeray, W. I. F. David, P. G. Bruce, J. B. Goodenough, *Mater. Res. Bull.* **1984**, *19*, 1497–1506.
[34] K. Ado, M. Tabuchi, H. Kobayashi, H. Kageyama, O. Nakamura, Y. Inaba, R. Kanno, M. Takagi, Y. Takeda, *J. Electrochem. Soc.* **1997**, *144*, L177-L180.
[35] M. N. Obrovac, O. Mao, J. R. Dahn, *Solid State Ionics* **1998**, *112*, 9–19.
[36] J. Lee, A. Urban, X. Li, D. Su, G. Hautier, G. Ceder, *Science* **2014**, *343*, 519–522.
[37] N. Yabuuchi, M. Nakayama, M. Takeuchi, S. Komaba, Y. Hashimoto, T. Mukai, H. Shiiba, K. Sato, Y. Kobayashi, A. Nakao, M. Yonemura, K. Yamanaka, K. Mitsuhara, T. Ohta, *Nat. Commun.* **2016**, *7*, 13814.
[38] M. Oishi, T. Fujimoto, Y. Takanashi, Y. Orikasa, A. Kawamura, T. Ina, H. Yamashige, D. Takamatsu, K. Sato, H. Murayama, H. Tanida, H. Arai, H. Ishii, C. Yogi, I. Watanabe, T. Ohta, A. Mineshige, Y. Uchimoto, Z. Ogumi, *J. Power Sources* **2013**, *222*, 45–51.
[39] M. Oishi, K. Yamanaka, I. Watanabe, K. Shimoda, T. Matsunaga, H. Arai, Y. Ukyo, Y. Uchimoto, Z. Ogumi, T. Ohta, *J. Mater. Chem. A* **2016**, *4*, 9293–9302.
[40] W. E. Gent, K. Lim, Y. Liang, Q. Li, T. Barnes, S.-J. Ahn, K. H. Stone, M. McIntire, J. Hong, J. H. Song, Y. Li, A. Mehta, S. Ermon, T. Tyliszczak, D. Kilcoyne, D. Vine, J.-H. Park, S.-K. Doo, M. F. Toney, W. Yang, D. Prendergast, W. C. Chueh, *Nat. Commun.* **2017**, *8*, 2091.
[41] M. Okubo, A. Yamada, *ACS Appl. Mater. Interfaces* **2017**, *9*, 36463–36472.
[42] S. L. Glazier, J. Li, J. Zhou, T. Bond, J. R. Dahn, *Chem. Mater.* **2015**, *27*, 7751–7756.
[43] E. McCalla, M. T. Sougrati, G. Rousse, E. J. Berg, A. Abakumov, N. Recham, K. Ramesha, M. Sathiya, R. Dominko, G. Van Tendeloo, P. Novák, J.-M. Tarascon, *J. Am. Chem. Soc.* **2015**, *137*, 4804–4814.
[44] D.-H. Seo, J. Lee, A. Urban, R. Malik, S. Kang, G. Ceder, *Nat. Chem.* **2016**, *8*, 692–697.
[45] A. R. Armstrong, M. Holzapfel, P. Novak, C. S. Johnson, S. H. Kang, M. M. Thackeray, P. G. Bruce, *J. Am. Chem. Soc.* **2006**, *128*, 8694–8698.
[46] M. Jiang, B. Key, Y. S. Meng, C. P. Grey, *Chem. Mater.* **2009**, *21*, 2733–2745.

 © 2019 The Chemical Society of Japan & Wiley-VCH Verlag GmbH & Co. KGaA, Weinheim

[47] H. Koga, L. Croguennec, P. Mannessiez, M. Ménétrier, F. Weill, L. Bourgeois, M. Duttine, E. Suard, C. Delmas, *J. Phys. Chem. C* **2012**, *116*, 13497–13506.
[48] N. Yabuuchi, Y. Tahara, S. Komaba, S. Kitada, Y. Kajiya, *Chem. Mater.* **2016**, *28*, 416–419.
[49] T. Matsuhara, Y. Tsuchiya, K. Yamanaka, K. Mitsuhara, T. Ohta, N. Yabuuchi, *Electrochemistry* **2016**, *84*, 797–801.
[50] G. G. Amatucci, J. M. Tarascon, L. C. Klein, *J. Electrochem. Soc.* **1996**, *143*, 1114–1123.
[51] L. Croguennec, C. Pouillerie, A. N. Mansour, C. Delmas, *J. Mater. Chem.* **2001**, *11*, 131–141.
[52] M. Nakajima, N. Yabuuchi, *Chem. Mater.* **2017**, *29*, 6927–6935.
[53] B. Ammundsen, J. Paulsen, I. Davidson, R.-S. Liu, C.-H. Shen, J.-M. Chen, L.-Y. Jang, J.-F. Lee, *J. Electrochem. Soc.* **2002**, *149*, A431–A436.
[54] J. R. Dahn, W. R. McKinnon, *Solid State Ionics* **1987**, *23*, 1–7.
[55] S. Hoshino, A. M. Glushenkov, S. Ichikawa, T. Ozaki, T. Inamasu, N. Yabuuchi, *ACS Energy Lett.* **2017**, 733–738.
[56] H. Arai, S. Okada, Y. Sakurai, J.-i. Yamaki, *J. Power Sources* **1997**, *68*, 716–719.
[57] M. Vlasse, J. C. Massies, G. Demazeau, *J. Solid State Chem.* **1973**, *8*, 109–113.
[58] A. Kitajou, E. Kobayashi, S. Okada, *Electrochemistry* **2015**, *83*, 885–888.
[59] R. Y. Chen, S. H. Ren, M. Knapp, D. Wang, R. Witter, M. Fichtner, H. Hahn, *Adv. Energy Mater.* **2015**, *5*, 1401814.
[60] N. Takeda, S. Hoshino, L. Xie, S. Chen, I. Ikeuchi, R. Natsui, K. Nakura, N. Yabuuchi, *J. Power Sources* **2017**, *367*, 122–129.
[61] A. K. Padhi, K. S. Nanjundaswamy, C. Masquelier, S. Okada, J. B. Goodenough, *J. Electrochem. Soc.* **1997**, *144*, 1609–1613.
[62] R. Shuhua, C. Ruiyong, M. Emad, D. Oleksandr, A. A. Guda, S. Viktor, W. Di, H. Horst, F. Maximilian, *Adv. Sci.* **2015**, *2*, 1500128.
[63] N. Yabuuchi, K. Yamamoto, K. Yoshii, I. Nakai, T. Nishizawa, A. Omaru, T. Toyooka, S. Komaba, *J. Electrochem. Soc.* **2013**, *160*, A39–A45.
[64] R. A. House, L. Jin, U. Maitra, K. Tsuruta, J. W. Somerville, D. P. Forstermann, F. Massel, L. Duda, M. R. Roberts, P. G. Bruce, *Energy Environ. Sci.* **2018**, *11*, 926–932.
[65] J. Lee, D. A. Kitchaev, D.-H. Kwon, C.-W. Lee, J. K. Papp, Y.-S. Liu, Z. Lun, R. J. Clément, T. Shi, B. D. McCloskey, J. Guo, M. Balasubramanian, G. Ceder, *Nature* **2018**, *556*, 185–190.
[66] S. H. Elder, L. H. Doerrer, F. J. DiSalvo, J. B. Parise, D. Guyomard, J. M. Tarascon, *Chem. Mater.* **1992**, *4*, 928–937.
[67] W. Xiao-Jun, K. Frank, W. Michael, N. Reinhard, J. Laurent, F. Helmer, *Chem. Eur. J.* **2012**, *18*, 5970–5978.
[68] N. Yabuuchi, R. Hara, M. Kajiyama, K. Kubota, T. Ishigaki, A. Hoshikawa, S. Komaba, *Adv. Energy Mater.* **2014**, *4*, 1301453.
[69] M. D. Slater, D. Kim, E. Lee, C. S. Johnson, *Adv. Funct. Mater.* **2013**, *23*, 947–958.
[70] K. Du, J. Zhu, G. Hu, H. Gao, Y. Li, J. B. Goodenough, *Energy Environ. Sci.* **2016**, *9*, 2575–2577.
[71] N. Yabuuchi, R. Hara, K. Kubota, J. Paulsen, S. Kumakura, S. Komaba, *J. Mater. Chem. A* **2014**, *2*, 16851–16855.
[72] B. Mortemard de Boisse, G. Liu, J. Ma, S.-i. Nishimura, S.-C. Chung, H. Kiuchi, Y. Harada, J. Kikkawa, Y. Kobayashi, M. Okubo, A. Yamada, *Nat. Commun.* **2016**, *7*, 11397.
[73] P. Rozier, M. Sathiya, A.-R. Paulraj, D. Foix, T. Desaunay, P.-L. Taberna, P. Simon, J.-M. Tarascon, *Electrochem. Commun.* **2015**, *53*, 29–32.
[74] K. Sato, M. Nakayama, A. M. Glushenkov, T. Mukai, Y. Hashimoto, K. Yamanaka, M. Yoshimura, T. Ohta, N. Yabuuchi, *Chem. Mater.* **2017**, *29*, 5043–5047.
[75] T. Sato, K. Sato, W. Zhao, Y. Kajiya, N. Yabuuchi, *J. Mater. Chem. A* **2018**, *6*, 13943–13951.
[76] A. Sakuda, T. Takeuchi, K. Okamura, H. Kobayashi, H. Sakaebe, K. Tatsumi, Z. Ogumi, *Sci. Rep.* **2014**, *4*, 4883.
[77] M. Freire, N. V. Kosova, C. Jordy, D. Chateigner, O. I. Lebedev, A. Maignan, V. Pralong, *Nat. Mater.* **2016**, *15*, 173–177.
[78] S. Okuoka, Y. Ogasawara, Y. Suga, M. Hibino, T. Kudo, H. Ono, K. Yonehara, Y. Sumida, Y. Yamada, A. Yamada, M. Oshima, E. Tochigi, N. Shibata, Y. Ikuhara, N. Mizuno, *Sci. Rep.* **2014**, *4*, 5684.
[79] H. Kobayashi, M. Hibino, Y. Ogasawara, K. Yamaguchi, T. Kudo, S.-i. Okuoka, K. Yonehara, H. Ono, Y. Sumida, M. Oshima, N. Mizuno, *J. Power Sources* **2016**, *306*, 567–572.
[80] K. Harada, M. Hibino, H. Kobayashi, Y. Ogasawara, S.-i. Okuoka, K. Yonehara, H. Ono, Y. Sumida, K. Yamaguchi, T. Kudo, N. Mizuno, *J. Power Sources* **2016**, *322*, 49–56.
[81] D. N. Mueller, M. L. Machala, H. Bluhm, W. C. Chueh, *Nat. Commun.* **2015**, *6*, 6097.
[82] A. Grimaud, W. T. Hong, Y. Shao-Horn, J. M. Tarascon, *Nat. Mater.* **2016**, *15*, 121–126.
[83] J. Lee, J. K. Papp, R. J. Clément, S. Sallis, D.-H. Kwon, T. Shi, W. Yang, B. D. McCloskey, G. Ceder, *Nat. Commun.* **2017**, *8*, 981.
[84] R. Fukuma, W. Zhao, M. Sawamura, Y. Noda, M. Harada, M. Nakayama, M. Goto, D. Kan, Y. Shimakawa, M. Yonemura, R. Watanuki, S. Fukuyama, Z. Han, H. Fukumitsu, M. Schulz-Dobrick, K. Yamanaka, T. Ohta, N. Yabuuchi, *submitted*.
[85] K. Momma, F. Izumi, *J. Appl. Crystallogr.* **2011**, *44*, 1272–1276.

Received: June 23, 2018
Accepted: September 26, 2018
Published online on October 12, 2018

 © 2019 The Chemical Society of Japan & Wiley-VCH Verlag GmbH & Co. KGaA, Weinheim